Momentum transfer driven by fluctuations in relativistic counter-propagating electron beams

A Ghizzo, D del Sarto

Momentum transfer driven by fluctuations in relativistic counter-propagating electron beams

A. Ghizzo[†], **D. Del Sarto**[*]

Institut Jean Lamour, UMR 7198, Lorraine University, CNRS, Campus ARTEM, BP 50840 54011 Nancy cedex, France

† Email address for correspondance: alain.ghizzo@univ-lorraine.fr

∗ Email: daniele.del-sarto@univ-lorraine.fr

January 2021

Abstract. A semi-Lagrangian relativistic Vlasov-Maxwell solver is used to describe the nonlinear momentum transfer between electron beams, which is driven by spontaneous fluctuations in the oblique filamentation instability (a type of Weibel mode) in two-dimensional plasmas. For counter-streaming plasmas, these filamentation instabilities may strengthen the generation of a fine structure of the distribution function in phase space. Properties of such counter-streaming beams are investigated using full-kinetic simulations and a Hamiltonian reduction technique based on the invariance of the transverse canonical momentum, the so-called multi-stream model. In the regime where $|\boldsymbol{k}|\, d_e \gg 1$, $\boldsymbol{k}$ being the wavevector and d_e the electron skin depth, a momentum transfer takes place when a mesoscale current filamentation mode couples with microscopic phase-space fluctuations. This regime is characterized by the appearance of filamentation modes with large wavenumbers and large amplitude fluctuations, which induce variations of the L^2-norm of the plasma in link with the self-organization of counter-streaming electron beams. We also discuss some theoretical aspects of information theory that highlight the role of the (reversible) entropy production in momentum transfer, thus by clarifying the connections between (microscopic) fluctuations of the distribution function and the fundamental aspects of the filamentation in Vlasov theory. The momentum transfer between beams is quantitatively analyzed by means of both theoretical estimations and numerical experiments.

1. Introduction

Instabilities driven by counter-streaming electron beams are a subject of relevance for many fields in plasma physics. The special case of relativistic counter-streaming electron beams is particularly relevant to the inertial confinement fusion or to the relativistic flows of astrophysical plasmas, in particular in the gamma ray-burst production scenario or in interpenetrating pulsar winds. Owing to the recent development of electromagnetic relativistic solvers and to the increased power of high performance computers, it has become possible to perform accurate numerical experiments of electromagnetic instabilities in counter-propagating relativistic beams in the laser-matter interaction

[1, 2, 3, 4, 5]. This has renewed the theoretical interest in these instabilities, especially in the nonlinear regime where the fluctuation level is high. Previous linear studies of Weibel-type instabilities [19, 8, 9, 10, 11, 47, 48] have identified different classes of electron beam-plasma instabilities: the current filamentation instability (here referred as CFI), the Weibel instability (WI), the electrostatic two-stream instability (TSI) and finally the oblique instability (OI). Such instabilities are considered as basic processes in a plasma since they are associated to the amplification of magnetic fields. WI is driven by thermal anisotropy in the plasma provided that the perpendicular temperature $T_\perp$ is larger than the parallel temperature $T_\parallel$, where $\perp$ and $\parallel$ represent the perpendicular and parallel direction with respect to the wave vector $\boldsymbol{k}$. While TSI modes are longitudinal (i.e. with $k_\perp = 0$), CFI modes are perpendicular (i.e. $k_\parallel = 0$). If perturbations both parallel and perpendicular to the beam flow become unstable, the instability is referred to as oblique. Moreover, a detailed analysis of the linear dispersion relation shows that oblique modes govern the system at high temperatures while CFI dominates in cold systems for counter-propagating beams carrying equal current densities.

More complex are the features of the saturation scenario of these instabilities.

It is well known that at small wavenumber $k = |k|$ (or large wavelength), i.e., for $kd_e \ll 1$, where $d_e = c\omega_p^{-1}$ is the electron skin depth, the growth of the magnetic field is limited by the Alfven mechanism [22]. The Alfven limit defines the maximum current that the electron can sustain before it is limited by particle trajectories in the self generated magnetic field (see also Ref. [24]). In the regime where $kd_e \gtrsim 1$, instead, the saturation of Weibel-type instabilities arises due to the magnetic trapping, a process that takes place when the magnetic bounce frequency is close to the linear growth-rate of the instability (see for instance Ref. [23]). In Ref. [20, 21] further saturation scenarii have been evidenced, which are related to the existence of newly observed time-resonant branches of filamentation oblique modes. These branches appear in counter-propagating electron beams, both in the $kd_e \gtrsim 1$ regime and in a new saturation regime, corresponding to $kd_e \gg 1$ and in which electrostatic trapping, instead of magnetic trapping, can be the dominant effect. In the $kd_e \gg 1$ regime, microscopic fluctuations are enhanced due to a possible transition of the oblique mode (usually occurring at a low wavenumber, i.e. with $kd_e \gtrsim 1$) to a new one that has a higher wavenumber.

It happens, then, that the simultaneous linear excitation of different branches of oblique modes can lead to different saturation regimes, depending on the kind of nonlinear coupling that takes place. This can be easily understood by a qualitative look at the contributions to the linear instability of the different terms of Vlasov equation.

From the point of view of a kinetic description based on Vlasov transport equation for the distribution function f, the linear growth of the initial perturbation is indeed related to the $\boldsymbol{v} \cdot \boldsymbol{\nabla}_x f$ "free streaming" term. Nonlinear mode coupling, related to the Lorentz force term $\boldsymbol{v} \times \boldsymbol{B} \cdot \boldsymbol{\nabla}_p f$, leads however to the transfer of energy to shorter wave lengths, where fluctuations are damped for k larger than a critical value k_{crit}, $k > k_{crit}$. As indicated by Medvedev and Loeb [25], balancing these two processes and replacing ∇_x with $k_{crit} \simeq k_{max}/\sqrt{2}$, where k_{max} is the wave number of the fastest growing mode,

gives an estimate of the amplitude of the steady magnetic field $\boldsymbol{B}$ at saturation of the $kd_e \gtrsim 1$ regime. The fact, however, that the linearly unstable perturbation can oscillate at larger wave-numbers, such as it happens for the low-frequency branch of oblique modes highlighted in Ref.[20], opens for the transition to saturation states where the free streaming term in Vlasov equation is not dominantly balanced by the Lorentz force term but rather by the electrostatic force term, $\boldsymbol{E} \cdot \boldsymbol{\nabla}_p f$.

In particular, since the oblique instability contains an electrostatic contribution, as met in TSI, the magnetic trapping may be already altered by the standard electrostatic particle trapping. In Ref.[21] this has been shown to occur, for example, in the so-called low-frequency regime of the oblique instability, where $kd_e \gg 1$ modes can be linearly destabilized, and for which magnetic trapping is also observed but is not the dominant saturation mechanism. Differently from what happens in the $kd_e \gtrsim 1$ regime of Weibel-type instabilities, magnetic trapping appears indeed as a transient process in the saturation regime of this oblique instability. The model of saturation by magnetic trapping is pertinent to the time development of the system during the first stage of the oblique mode instability, and is valid as long as the level of fluctuations has not changed substantially in the system: when a transition of the low-frequency oblique filamentation mode, initially generated in the domain where $kd_e \gtrsim 1$, arises and leads by nonlinear coupling to the excitation and growth of a large wavenumber mode having $kd_e \gg 1$, an oscillatory transfer between the magnetic and the kinetic energy components takes place. The observed transition is accompanied by an amplification of fluctuations in the configuration space, mainly at the microscopic level.

This amplification of fluctuations gives rise to a self-organization of the plasma and to a momentum transfer, as well as to a violation of Casimir invariants in presence of large amplitude spontaneous fluctuations (despite the Hamiltonian character of the system). This phenomenon, namely the fact that the nonlinear rearrangement of the Vlasov plasma could not respect anymore the invariance of Casimir when the distribution function is coarse-grained, i.e. it is viewed through a "finite-size granularity", is already known in plasma turbulence [35].

In this paper we discuss how a process analogous to the "granularity problem" in tokamak plasma turbulence occurs in configurations relevant to laser-plasma interactions or to relativistic plasma jets in astrophysics. In particular, we discuss the momentum transfer occurring in instabilities of counter-streaming electron beams when self-organization, triggered by microscopic fluctuations of the distribution function, takes place. We investigate this problem both in the classical and fully relativistic limit, the latter being identified by the fact that both the beams' velocity and thermal energy becomes relativistic. In this way we complement the numerical analysis performed in a previous paper [21], where reversible macroscopic entropy fluctuations have been evidenced only for relativistically streaming beams with non relativistic temperatures. In the aforementioned paper it was discussed how the *spatial filamentation* process due to electrostatic fluctuations, which are associated to the excitation of high-wavenumber oblique instabilities, can compete with the kinematic filamentation process of the

distribution function f in the velocity space (the latter being linked to the concept of regularity of f itself). It is such a filamentation process in the coordinate space that can lead to a reversible entropy growth, which is very different from the usual loss of information due to (numerical) coarse-graining effects that is instead inherently irreversible in nature. The spatial filamentation process related to the excitation of high-wavenumber oblique modes is similar to the inverse-cascade scenario met in turbulence. In the present article we discuss the analogies of spatial filamentation with the granularity scenario by focussing on the role played in it by the nonlinear momentum exchange between particles.

The paper is structured as follows. In Sec. II we discuss some aspects of the Vlasov-Maxwell model and of the analytical theory related to the Hamiltonian reduction technique of interest here, namely the "multi-stream" model, in link with the invariance of generalized (perpendicular) canonical momenta. Sec. III is devoted to the momentum transfer mechanism and to the violation of Casimir invariants observed in the self-organization of the plasma, which is associated to spontaneous microscopic fluctuations. Comparisons between theory and numerical experiments, carried out with a collisionless, "noiseless" semi-lagrangian Vlasov-Maxwell solver are then made in sec. IV, in both the classical and relativistic regime of the counter-propagating beam-plasma system. Conclusions are in Sec. V. In Appendix A we discuss how large amplitude fluctuations of the distribution function can be quantitatively related to macroscopic, reversible entropy fluctuations (of non-numerical nature) via arguments based on information theory.

2. The Vlasov-Maxwell model and its properties

2.1. The full kinetic description of the physical model

We start by considering the Hamiltonian of a particle in a two-dimensional system,

$$H = mc^2 \left(\gamma - 1\right) + e\phi \left(\boldsymbol{x}, t\right) \tag{1}$$

where ϕ is the electrostatic potential and $e < 0$ is the electron charge. In (1) the Lorentz factor is given by $\gamma = \sqrt{1 + \frac{\boldsymbol{p}^2}{m^2 c^2}}$. Note that $\boldsymbol{p}$ is the kinematic relativistic momentum, which is related to the canonical momentum in phase-space by

$$\boldsymbol{P}_c = \boldsymbol{p} + e\boldsymbol{A}\left(\boldsymbol{x}, t\right), \tag{2}$$

where $\boldsymbol{A}$ is the electromagnetic vector potential. We assume ions to constitute an infinitely massive, uniform background. This is a valid approximation since, for realistic ion masses, the ion motion would not participate in the instability on the time scale of interest here.

The evolution of a collection of particles, say electrons, is described in statistical terms by the distribution function $f = f\left(\Gamma, t\right)$, where $\Gamma = \left(\boldsymbol{x}, \boldsymbol{p}\right)$ is a shortened writing for the domain of the distribution function with respect to the spatial coordinate and kinematic momentum. In absence of collisions the Vlasov equation reads

$$\frac{\partial f}{\partial t} + \left\{f, H\right\} = 0, \tag{3}$$

where,

$$\boldsymbol{E} = -grad\,\phi + \frac{\partial \boldsymbol{A}}{\partial t}, \qquad \boldsymbol{B} = rot\,\boldsymbol{A}. \tag{4}$$

The Poisson brackets are defined as usual by $\{f, H\} = \frac{\partial f}{\partial \boldsymbol{x}} \cdot \frac{\partial H}{\partial \boldsymbol{p}} - \frac{\partial f}{\partial \boldsymbol{p}} \cdot \frac{\partial H}{\partial \boldsymbol{x}}$. The electromagnetic field $(\boldsymbol{E}, \boldsymbol{B})$ obeys Maxwell's equations:

$$\frac{\partial \boldsymbol{E}}{\partial t} - c^2 rot\boldsymbol{B} + \frac{\boldsymbol{J}}{\varepsilon_0} = 0 \tag{5}$$

$$\frac{\partial \boldsymbol{B}}{\partial t} + rot\boldsymbol{E} = 0 \tag{6}$$

$$div\boldsymbol{E} = \frac{\rho}{\varepsilon_0} \tag{7}$$

$$div\boldsymbol{B} = 0 \tag{8}$$

where the electron current density $\boldsymbol{J}$ and the charge density ρ (n_0 being the fixed background ion density) are given by:

$$\boldsymbol{J} = \int \frac{\boldsymbol{p}}{m\gamma} f d^3p \tag{9}$$

$$\rho = e \int f d^3p - e n_0 \tag{10}$$

For the kind of problem we are going to study we can consider a two-dimensional configuration in space with periodic boundary conditions in both x and y directions and two dimensions in the momentum space, i.e. we have $\boldsymbol{x} = (x, y)$ and $\boldsymbol{p} = (p_x, p_y)$.

It is informative to summarize some general properties of Eqs. (3) - (10).

(i) The Vlasov-Maxwell (VM) system implies the following integral relation:

$$\frac{\partial}{\partial t}\left(\int mc^2\,(\gamma - 1)\, f d^2p + \frac{1}{2}\varepsilon_0 E^2 + \frac{B^2}{2\mu_0}\right) + div\left(\int mc^2\,(\gamma - 1)\,\frac{\boldsymbol{p}}{m\gamma} f d^2p + \frac{\boldsymbol{E}\times\boldsymbol{B}}{\mu_0}\right) = 0. \tag{11}$$

Eq. (11) expresses the familiar local conservation of the total particle kinetic energy density plus the electromagnetic energy density. Moreover, when the divergence term vanishes, such as for periodic boundary conditions, Eq. (11) leads to the conservation of the total energy.

(ii) The further conservation of $\int d\Gamma \mathcal{F}(f)$, with $\mathcal{F}$ arbitrary function of f, is also granted, provided that f is a regular solution of the VM system (see point (iii) below). These integrals are usually called *Casimir's invariants*, and their conservation follows from the invariance of Vlasov equation under time reversal and from the fact that they commute, by construction, with the Hamiltonian. Of particular interest to us are the L^2-norm, defined as $L(f) = \int d\Gamma f^2$ and the L^∞- norm which, multiplied by k_B, corresponds to Shannon's entropy $S(t) =$

$-k_B \int d\Gamma f \ln f$. Both functions S and L, being convex functional of f, can be viewed as entropy-like quantities: the functional S gets its main contribution from smaller values of f, that is from particles close to the tails of the distribution function, whereas the bulk of the distribution mostly contributes to L.

(iii) From a mathematical point of view, regular solutions of the VM system are defined, following the works of Diperna and Lions in Ref. [12] (see also the works of Villani in [13] for the Landau damping problem and the works of Rein in [14] for the relativistic treatment of the VM system), as solutions that are "weakly convergent" in the sense of distributions. This implies they must have "*a limited amount of regularity of* f" (see the aforementioned references).

(iv) From the physical point of view, a given volume in the phase-space may be stretched and twisted by the incompressible flow, and Liouville's theorem states that the measure of the volume remains unchanged during the evolution of the VM plasma. The distortion of the volume in which f is non-zero gives rise to the so-called *(kinetic) filamentation process of* f in the velocity space (which is actually different from the so-called (current) filamentation process met in Weibel-type instabilities). Therefore, strong relativistic effects, such as those which are expected in the Weibel-type instabilities, can push the Vlasov model to its ultimate limits, by enhancing the intrinsic (Vlasov) filamentation process and therefore by altering the "weak convergence" properties of the VM solution.

(v) From the point of view of statistical mechanics, entropy plays a major role because of its connection with information theory and, despite the collisionless Hamiltonian nature of the Vlasov model, it provides a source of many questions in plasma physics. Since Boltzmann work on H-theorem and subsequent Shannon's theorem in information theory, entropy should be indeed regarded not as an intrinsic physical quantity of the system, but rather as a measure of the information that an observer can extract from it. And since the Vlasov-Maxwell plasma is a conservative system, from a thermodynamical point of view its entropy should remain constant in time. We then argue from the time-reversal invariance of the VM system that a complete microscopic description of a closed Vlasov plasma cannot loose information. However, from the point of view of statistical physics, the entropy may increase even in a closed conservative, deterministic system, when the information "stored" in the initial conditions is made irrelevant by chaotic or turbulent motion. Analogously, entropy generally increases in coarse-grained systems when microscopic degrees of freedom are ignored (or when discrete variables are used to describe a continuum phase space, such as it happens in the numerical approach). Of course, this latter occurrence is also observed in the numerical description of Vlasov plasmas. The point of interest, here, is what can happen when the loss of the regularity of the VM system solution (point (ii)) does not grant anymore the conservation of Casimirs (point (iii)) because of the effect of phase-space filamentation (point (iv)): reversible, large amplitude entropy fluctuations

can occur. In the following (Sec. III and Appendix A) we are going to highlight this point.

2.2. Hamiltonian reduction technique: the multi-stream (MS) approach:

In order to quantitatively address the relation between the momentum transfer and the violation of Casimirs' conservations, and in particular of the L^2-norm, we will make use of a Hamiltonian reduction technique, the multi-stream (MS) approach [17, 18]. This model is based on the existence of cyclic space variables, and on the invariance of the components of the canonical momentum $\boldsymbol{P}_{c\perp} = \boldsymbol{p}_\perp + e\boldsymbol{A}_\perp(x,t)$ transverse to them, i.e. orthogonal to $\boldsymbol{k}$ in an initially homogeneous beam. In he remainder of this Section II.2 and in the numerical applications of Sec. IV.1.2 we focus on the case in which the only non-cyclic coordinate is for example x, which is appropriate for the study of pure CFI modes destabilized when beams propagate, e.g., along y direction.

A direct comparison between the multi-stream model and a full 1D2V semi-lagrangian numerical model for the CFI has been already discussed in Ref.[15]. In this article we focus on the insight that the use of canonical invariants to describe the particle dynamics gives on the momentum transfer occurring in the CFI.

To this purpose, let us first recall the main properties of this Hamiltonian reduction technique. To this end, consider a collection of N_s bunches of particles, each "stream" j, with $1 \leq j \leq N_s$, having the same initial perpendicular momentum $\boldsymbol{P}_{c\perp} = \boldsymbol{C}_j = const.$ For each particle population j we can introduce a reduced Vlasov-type equation and a distribution function $f_j(x, p_x, t)$. The corresponding Hamiltonian of a single particle belonging to the stream j is given by

$$H_j = mc^2(\gamma_j - 1) + e\phi(x,t) \tag{12}$$

with Lorentz' factor

$$\gamma_j = \sqrt{1 + \frac{p_x^2}{m^2c^2} + \frac{\left(\boldsymbol{C}_j - e\boldsymbol{A}_\perp(x,t)\right)^2}{m^2c^2}} \tag{13}$$

In Coulomb's gauge $div\boldsymbol{A} = 0$ we can write $\boldsymbol{A} = \boldsymbol{A}_\perp$ and the Hamilton equation $d\boldsymbol{P}_c/dt = -\partial H_j/\partial \boldsymbol{x}$ splits into the longitudinal part $dP_{cx}/dt = -\partial H_j/\partial x$ and the perpendicular part $d\boldsymbol{P}_{c\perp}/dt = -\partial H_j/\partial \boldsymbol{x}_\perp = 0$. The distribution function f_j satisfies therefore the reduced Vlasov equation

$$\frac{\partial f_j}{\partial t} + \frac{p_x}{m\gamma_j}\frac{\partial f_j}{\partial x} + \left[eE_x - \frac{1}{2m\gamma_j}\frac{\partial}{\partial x}\left(\boldsymbol{C}_j - e\boldsymbol{A}_\perp(x,t)\right)^2\right]\frac{\partial f_j}{\partial p_x} = 0. \tag{14}$$

Equation (14) is then coupled, in a self-consistent way, with Maxwell's equations. The potential vector $\boldsymbol{A} = \boldsymbol{A}_\perp(x,t)$ and the longitudinal electric field E_x satisfy, respectively:

$$\frac{\partial^2 \boldsymbol{A}_\perp}{\partial t^2} - c^2\frac{\partial^2 \boldsymbol{A}_\perp}{\partial x^2} = \frac{\boldsymbol{J}_\perp}{\varepsilon_0} = \frac{1}{\varepsilon_0}\sum_{j=1}^{N_s}\boldsymbol{J}_{\perp j} \tag{15}$$

$$\frac{\partial E_x}{\partial x} = \frac{e}{\varepsilon_0}\left(n\left(x,t\right) - n_0\right) = \frac{e}{\varepsilon_0}\left(\sum_{j=1}^{N_s} n_j - n_0\right) \tag{16}$$

For each population j we have defined a density as $n_j = \int f_j dp_x$ and a current density $\boldsymbol{J}_{\perp j} = \frac{e}{m}\left(\boldsymbol{C}_j - e\boldsymbol{A}_\perp\right)\int dp_x f_j/\gamma_j$.

One could approximate any kind of equilibrium distribution with a sufficient number of "streams". As shown in Ref.[15], the MS model is capable of capturing the main features of the physics of Weibel-type instabilities, even during the nonlinear regime, and even when a small number of streams are used.

In next Section 3 we are going to use this reduction technique to characterize the nature of the momentum transfer.

3. Momentum transfer in filamentation-type instabilities

In the Vlasov dynamics, there is a great deal of stretching and twisting of each elementary parcel or "fluid" in the phase-space, with the result that large amplitude gradients locally develop in some regions of the domain. So, what does it happen when a physical instability locally alters or even strengthen the kinetic filamentation process of f in velocities, by thus perturbing the "smooth" (or regular) character of the distribution function? This is the question we are going to address in this Section, with reference to the $kd_e \gg 1$ regime of the instability previously mentioned (Sec. 1).

The impact that filamentation has on the mean velocity of beams in the regime of large amplitude fluctuations of the distribution function is presented in Appendix A. A drift in beam velocity is observed (and referenced by the δV_y quantity afterwards). It corresponds to a transfer of momentum between the beams which occurs in a quasi-symmetrical way. Microscopic fluctuations of the distribution function can indeed play the role of two-particle correlations and filamentation can cause momentum transfer associated to fluctuations of the L^2-norm.

The fluctuations δf_1 in Eq. (A.1) which are responsible of the time variation of the L^2 norm (see Eq. (A.5)) and of analogous Casimir's invariants of f_1, are also a source of pseudo-momentum. Let us now explore in detail the momentum transfer associated to these fluctuations.

To this purpose, it is instructive to discuss an example in which the momentum transfer related to fluctuations occurs in a classical context. We then consider a given beam of velocity v_j (for $j = 1, 2$) and we follow the lines of the analysis developed for kinetic turbulence in tokamak plasmas by Diamond et al. [35]: we expand f_1 near a coherent phase space structure, propagating at a phase velocity close to the beam velocity, $v_\varphi \simeq v_j$ (in the so-called "phasestrophy" concept met in tokamak plasma turbulence, these structures are sometimes referred to as "granulations" of the phase-space). Naming $\Gamma = (\boldsymbol{x}, \boldsymbol{v})$ and $\Gamma_j = (\boldsymbol{x}, \boldsymbol{v_j})$ and assuming the phase velocity to have

components $v_{\varphi x}=0$ and $v_{\varphi y}=v_j$, we write:

$$\overline{f_1}\left(\Gamma,t\right)=\overline{f_1}\left(\Gamma_j,t\right)+\left(v_x-v_{\varphi x}\right)\left.\frac{\partial\overline{f_1}}{\partial v_x}\right|_{\Gamma=\Gamma_j}+\left(v_y-v_{\varphi y}\right)\left.\frac{\partial\overline{f_1}}{\partial v_y}\right|_{\Gamma=\Gamma_j}. \tag{17}$$

Assuming in Eq.(A.7) the conservation of the contribution $L\left(f_1\right)$ in L_2, and assuming $\delta V_x\simeq 0$, we obtain

$$\begin{aligned}\frac{\partial\delta L}{\partial t}&=-2\frac{\partial}{\partial t}\left(\int d\Gamma\left(v_y-v_b\right)\left\langle\delta f\left(\Gamma/\Gamma_2\right)\right\rangle_{\Gamma_2}\left.\frac{\partial\overline{f_1}}{\partial v_y}\right|_{\Gamma=\Gamma_j}\right)\\&=-2\left.\frac{\partial\overline{f_1}}{\partial v_y}\right|\frac{\partial\delta V_y}{\partial t},\end{aligned} \tag{18}$$

where

$$\boldsymbol{V}\equiv\int d\Gamma_1\boldsymbol{v}\left\langle\delta f\left(\Gamma_1/\Gamma_2,t\right)\right\rangle_{\Gamma_2}\text{ and }\delta V_y=V_y-v_j. \tag{19}$$

$\boldsymbol{V}$ is the mean velocity associated to the distribution function δf at the microscopic scale while δV_y is the variation of the relative mean velocity with respect to the initial beam velocity v_j. For a single species plasma, the momentum conservation typically requires $dV_y/dt=0$. This means that no fluctuations are usually observed and, e.g., mobile ions are required so to grant this condition if the beam is constituted by electrons (and vice-versa).

The situation is somehow different when two counter-streaming electron beams are considered, since a new degree of freedom is in this way introduced by allowing the momentum transfer from one electron beam to another. In the case of two counter-streaming beams with opposite velocities $\pm v_1$ moving along y, it is possible to estimate the mean velocity variation by integrating

$$\frac{1}{c}\frac{\partial\delta V_y}{\partial t}=-\frac{\int\frac{d\Gamma_1}{L_0}\left\langle\delta f\left(\Gamma_1/\Gamma_2,t\right)\right\rangle_{\Gamma_2}^2}{\left.\frac{2}{f_0}\frac{\partial\overline{f}}{\partial\beta_y}\right|_{\beta_j}}, \tag{20}$$

if we assume a linear "L^2-entropy" variation versus time: in particular, in (20) we have assumed $L=L_0(1+\sigma t)$ where $\sigma=\frac{1}{L_0}\frac{\partial L}{\partial t}$ is the "L^2-entropy" loss rate ($\sigma<0$) , and L_0 and f_0 are the initial "L^2-entropy" and distribution function corresponding to the initial equilibrium, respectively. Here we have introduced the notation $\beta=v/c$ for the velocity normalized to the light velocity c. Integration of Eq.(20) over time leads to

$$\frac{\delta V_y\left(t\right)}{c}=\frac{\sigma t}{\left.\frac{2}{f_0}\frac{\partial\overline{f}}{\partial\beta_y}\right|_{\beta_j}} \tag{21}$$

In Eq. (21), we can estimate $\left.\frac{1}{f_0}\frac{\partial\overline{f}}{\partial\beta_y}\right|_{\beta_j}=\frac{\beta_j}{\beta_{Ty,j}^2}$, where $\beta_j=v_j/c$ and $\beta_{Ty,j}=v_{Ty,j}/c$ represents the beam velocity and the thermal velocity component along the beams

respectively, normalized with respect to the velocity of light. This result shows that the large amplitude fluctuations at microscopic scales, which can be encountered in the $kd_e \gg 1$ regime of the oblique instability, when filamentation modes with large wavenumber appear, not only can induce variations of the quantity L as shown in Ref.[21], but can be also a source of pseudo-momentum. The presence of a multi-scale dynamics in plasmas generally allows the interaction between instabilities occurring at different scales. In particular, fluctuations with respect to the space coordinate at large wavenumbers of the oblique instability (e.g. at $kd_e \gg 1$) can be also a source for spatial fluctuations of the distribution f_1 at small wavenumbers (or low-frequencies). This generates a stress (or pressure) tensor, which in turn acts upon these modes by generating fluxes in momentum. On the other hand, as shown in [36], a feedback of larger scale "coherent" structures on small scales is also possible. The generation of a stress (or pressure) tensor, which influences the mean particle motion and which is due to spatial inhomogeneities of the distribution function that are related to the presence of mean shear flows, had been shown also in a fluid description extended to include the full pressure tensor dynamics [37, 38].

Most of the existing analytical studies of turbulence-driven effects in Vlasov models focus on the concept of "granulations" in the phase space of magnetically confined plasmas [41], or on the nonlinear excitation of shear flows by the Reynolds stress dynamics [36, 39, 40]. In tokamak plasmas dominated by drift-wave/zonal-flow turbulence, the small-scale drift-waves induce the transport of momentum triggered by the Reynolds stress. The energy of drift-waves is then transferred to zonal flows, so that the level of small-scale fluctuation and the associated transport are reduced. This is an important nonlinear process for the self-organization and confinement of toroidal magnetized plasmas.

In the following, we consider an analogous coupling involving different filamentation (Weibel-type) instabilities, namely CFI, Weibel instability and OI, that develop at different spatial and frequency scales. In this, we will carefully consider the role played by spatial fluctuations at the microscopic scale of the electromagnetic (current) filamentation instability. Through this process, which takes place in counter-propagating electron beams, the feedback loop between the transition from the small wavenumber to the large wavenumber component of filamentation-type modes and entropy-type (L or L^2- norm) fluctuations becomes manifest. This loop gives rise to an elementary process in which momentum transfer is involved.

4. Numerical simulations

In this Section we compare the theoretical predictions of Sec. III with the results of computer simulations performed with the full relativistic, electromagnetic semi-Lagrangian Vlasov ElectroMagnetic (VLEM) solver [42], which integrates the Vlasov equation by direct discretization of the phase space. The trajectories of particle motion (the so-called characteristics) are determined from the self-consistent electromagnetic

fields using full relativistic dynamics equations. This Vlasov-Maxwell code uses a standard time splitting scheme, local Hermite and global cubic spline or B-spline interpolation techniques. These have been adapted so to optimally use distributed computational environments in high performance computing. Further details on the solver can be found in Ref. [42].

For the problem we are interested in we can restrict to a two-dimensional (2D2V) or even to a $1D\frac{1}{2}$ geometry (i.e., 1D2V) geometry −see each specific case, below−, in which the relevant components of the electromagnetic fields are $\boldsymbol{E} = (E_x, E_y, 0)$ and $\boldsymbol{B} = (0, 0, B_z)$. In all simulations presented here, the "plasma plus beam system" consists of two electron beams with densities n_1 and n_2, and velocities $v_1 = \beta_1 c \leq 0$ and $v_2 = \beta_2 c \geq 0$ propagating in the y direction. Charge and current neutrality is ensured by requiring $n_1 + n_2 = n_0$ and $n_1\beta_1 + n_2\beta_2 = 0$. Ions form a fixed neutralizing background and collisions are neglected.

In the code, normalized quantities are used, which is why in the following we will sometimes refer to adimensional values while interpreting the results or describing the setup: time t, the space coordinate $\boldsymbol{x}$ and momentum $\boldsymbol{p}$ are respectively normalized to the inverse plasma frequency ω_p^{-1}, to $c\omega_p^{-1}$ and to mc. The electric and magnetic field vectors are respectively normalized to $m\omega_p c/e$ and $m\omega_p/e$.

4.1. Momentum transfer in classical counter-streaming beams

4.1.1. CFI-WI modelling via 1D2V semi-Lagrangian simulation We have performed a first numerical simulation using an initial condition characterized by two symmetric electron beams (i.e. with $n_1 = n_2$). The considered geometry in this subsection is 1D2V, i.e. one spatial dimension, say x, and two variables in momentum p_x and p_y. The CFI is produced by the electromagnetic interaction of two counter-propagating electrons beams of velocity $v_1 = -0.35c$ and $v_2 = 0.35c$, of identical temperatures of $T_{1x} = T_{2x} = 2keV$ along the x direction. In order to couple CFI with WI we have also introduced a temperature anisotropy by setting a temperature of $T_{1y} = T_{2y} = 4keV$ in the direction of propagation of the beams. This initial configuration is non relativistic and the initial equilibrium consists therefore of two drifted Maxwellians. The numerical domain has extension $L_x = 2\pi c\omega_p^{-1}$ in space and, with respect to the momentum coordinate, we fixed a cut-off for $|p_x/mc| \leq 1.25$ and $|p_y/mc| \leq 1.25$. The magnetic perturbation is introduced in the B_z component of the magnetic field and corresponds to a pure sine function of type $B_0 \sin k_0 x$, with a perturbation amplitude of eB_0/mc of 10^{-5} in normalized units and $k_0 c/\omega_p = 1$. Note that the wave vector $\boldsymbol{k} = k_0 \boldsymbol{e}_x$ is along the x direction perpendicular to counter-propagating beams.

Such a system, due to the simultaneous presence of counter-streaming electron beams and temperature anisotropy (with $T_{1;2y} > T_{1;2x}$) allows to couple CFI and WI. This increases the linear growth-rate of the resulting instability [43], which amplifies spontaneous magnetic fluctuations (see Refs. [4, 44, 45, 46]).

Numerical results corresponding to the full 1D2V kinetic simulation are shown in

Figs. 1 -3. On top panel, in Fig. 1, we have plotted the square root of the magnetic energy $\sqrt{\varepsilon_m}$ versus time. As expected, the CFI-WI coupling proceeds through the linear stage for $40 \leq t\omega_p \leq 60$, in which the magnetic energy grows exponentially in time, and is followed by the nonlinear saturation where magnetic trapping takes place. The bounce magnetic frequency ω_B is in good agreement with the expected value of

$$\frac{\omega_B}{\omega_p} = \sqrt{\frac{k_0 c}{\omega_p}\frac{p_2}{mc\gamma_2^2}\frac{eB_{max}}{m\omega_p}} = \sqrt{1 \times 0.370 \times 0.21} \simeq 0.278. \tag{22}$$

This value corresponds to a bounce period $T_B = 2\pi/\omega_B \simeq 22.5\omega_p^{-1}$.

We have superimposed the corresponding bounce period on the time evolution of $\sqrt{\varepsilon_m}$ on top panel in Fig. 1. While the quantity $\sqrt{\varepsilon_m}$ exhibits clearly an oscillatory behavior at the bounce magnetic frequency ω_B just after the saturation, another high frequency component is clearly visible which seems dominate in the asymptotic time. Thus, the long time behavior appears to be affected by the CFI-WI coupling and the emergence of magnetic fluctuations. The $x - p_x$ phase space representation, shown on bottom panels in Fig. 1, reveals the formation of two magnetic trapping vortices, at time $t\omega_p = 60$ (at left), with a phase velocity close to $v_\varphi = \omega_{CFI}/k_0 \simeq 0$, but such a process is stopped rapidly (magnetic trapping structures have disappeared at time $t\omega_p = 80$). Such vortices have modified the nonlinear stage of the instability enough, so that an electrostatic field starts to grow near saturation leading to a coupling with Langmuir waves.

In Fig. 2 we have plotted the time evolution of the total energy, which remains constant during the simulation to within 0.02%. This clearly shows the excellent energy conservation even in the strongly nonlinear regime of the interaction. Notice that a high-frequency oscillatory behavior due to the electrostatic component (close to a frequency $\omega \sim 1.2\omega_p$, that is, well above the bounce magnetic frequency) is observed after saturation.

On top and middle panels in Fig. 3, we have represented the contour plot of the distribution function in the $(\boldsymbol{x}, \boldsymbol{p})$-space at times $t\omega_p = 0$ (initial time) and $t\omega_p = 200$ (final time), which highlights the momentum transfer observed in the simulation. Fig. 3 gives an illustration of the particle dynamics in the $p_x - p_y$ momentum plane (on top panels) and in the $x - p_y$ phase space (on middle panels) respectively. While the distribution $f(x, p_y)$ has been averaged over the p_x coordinate, the data of $f(p_x, p_y)$ is given at the middle of the box ($x = L_x/2$). Due to the modulation driven by the electromagnetic field, a momentum transfer is produced between beams leading to a modification of their mean velocity. Such a modulation is clearly visible in Fig. 3. Notice that a flattening of the velocity profile along p_x, corresponding to a "heating", can be observed.

From the numerical data provided by the Vlasov code, it is possible to model the shape of the distribution that results at the time $t\omega_p = 200$ of the transport process. The transfer of momentum is associated with a modification of the beam distribution of velocity β_1. In the lower panel in Fig. 3, we have represented by circles the shape of

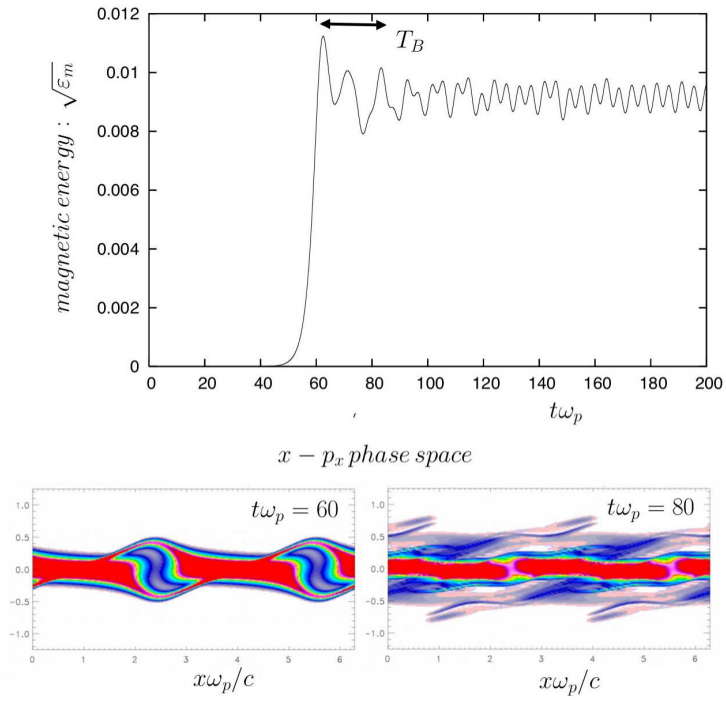

Figure 1. On top panel: plot of the square root of the magnetic energy $\sqrt{\varepsilon_m}$ versus time. The magnetic bounce period estimated from Eq.(22) is also indicated. On bottom panel: $x - p_x$ contour-plot representation of f at two different times. The simulation, performed using the 1D2V version of the VLEM solver, corresponds to the case of CFI-WI coupling discussed in Sec.4.1.1. Here we have used $T_{2y} = T_{1y} = 4keV$ for the perpendicular temperature of beams and $\beta_2 = -\beta_1 = 0.35$ for velocities.

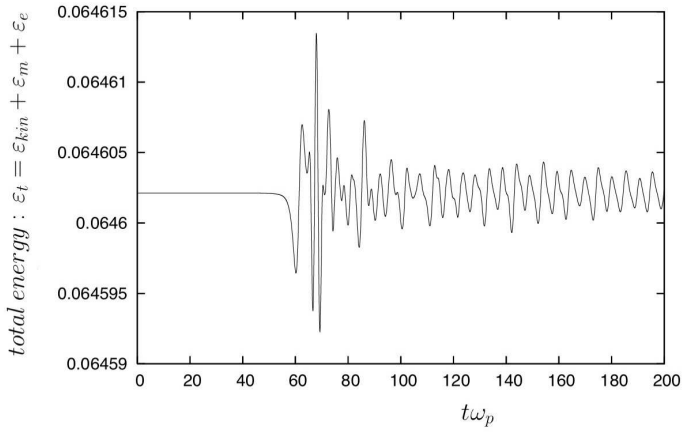

Figure 2. Time variation of the total energy. Note the excellent conservation within a 0.02% during the whole simulation. The figure corresponds to the simulation results of Fig. 1 for the study of the CFI-WI coupling. Here we have used $T_{2y} = T_{1y} = 4keV$ for the perpendicular temperature of beams and $\beta_2 = -\beta_1 = 0.35$ for velocities.

the smoothed $\overline{f}$ distribution of the beam (of negative velocity) with respect to the maxwellian distribution (here represented in solid line). The function $\overline{f}$ takes the following expression:

$$\overline{f} \sim \frac{(v_y + v_1)^2}{2v_{Ty,1}^2} \frac{1}{\sqrt{2\pi} v_{Ty,1}} e^{-\left(\frac{(v_y - v_1)^2}{2v_{Ty,1}^2}\right)} \tag{23}$$

From (23) we can estimate the normalized quantity

$$\frac{1}{f_0} \frac{\partial \overline{f}}{\partial \beta_y}\bigg|_{\beta_1} = \frac{\beta_1}{\beta_{Ty,1}^2}. \tag{24}$$

In order to have an estimate of variation of the mean velocity of a given beam, we have plotted the time evolution of the quantity L (the L^2- norm) on top panel in Fig. 4 (notice the linear decrease of L at saturation). On bottom panel, we have represented the mean velocity variation δV_y (normalized to the light velocity) defined by the relation

$$\delta V_y = \frac{1}{L_x L_y} \int_0^{L_x} dx \int_0^{L_y} dy \int_{-\infty}^{+\infty} dp_x \int_0^{+\infty} dp_y \left(\frac{p_y}{m\gamma} - v_2\right) f \tag{25}$$

Notice that similar expression may be obtained for the other beam, which indeed is symmetric. In the classical case, the decrease in the average velocity of one of the beams corresponds roughly to the increase of the other (the sum of these two quantities can be considered as a Casimir's invariant which remains well preserved in the code). Using Eq. (21) we can estimate the normalized velocity variation δV_y of the beam $j = 2$ as:

$$\frac{\delta V_y}{c} = \frac{\sigma \Delta_t}{\frac{2}{f_0} \frac{\partial \overline{f}}{\partial \beta_y}\Big|_{\boldsymbol{\beta}=\beta_2}} = \frac{\sigma \Delta_t T_{1y}}{4\beta_2 mc^2} \sim -\frac{0.22 \times 70 \times 2.5}{4 \times 0.35 \times 511} \simeq -0.107 \tag{26}$$

In Eq. (26), the rate at which "entropy" is lost is close to $\sigma = \frac{5.6-7.2}{7.2} = -0.22$ during the time interval $\Delta_t = 70\omega_p^{-1}$, while the estimated temperature of the beam is $T_{1y} \sim T_{2y} \sim 2.5keV$, in the asymptotic regime, where the Weibel instability has saturated.

On bottom panel in Fig. 4, the evolution of $\delta V_y = V_y - v_2$, obtained from (25) clearly shows a drift in the mean velocity in good agreement with the expected estimation. The emphasis is here on the positive velocities in v_y of particles. Note that the contribution of the Poynting vector remains negligible.

The results of the nonlinear 1D2V Vlasov simulations show that the nonlinear saturation is governed by the nonlinear momentum transfer and that the magnetic trapping, although occurring at the beginning of the saturation mechanism, is not the dominant process in the asymptotic regime: the self-organization of the system constituted by two counter-streaming electron beams begins with a nonlinear, symmetry-breaking momentum transfer, where the plasma adjusts itself in wave number so to give a stable state dominated by trapping of both electric and magnetic nature.

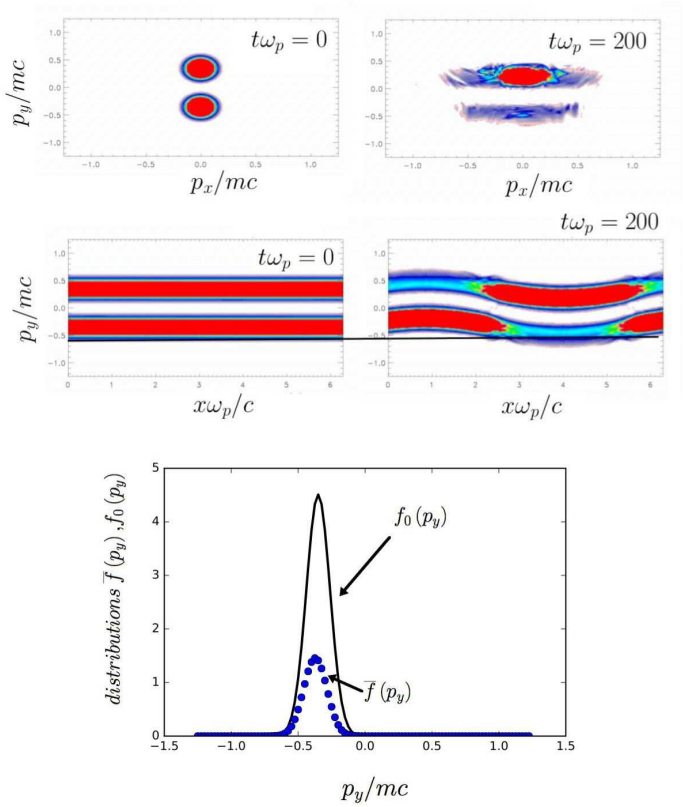

Figure 3. On top panels: plot of the distribution function in the $p_x - p_y$ momentum space, computed at $x = L_x/2$. On middle panels, the corresponding $x - p_y$ phase space representation of the distribution function, averaged over p_x, for the CFI-WI coupling. On bottom panel, test functions showing the averaged distribution of the first beam (of velocity $\beta_1 < 0$) as a function of the p_y component, at the initial equilibrium f_0 (represented by a Maxwellian distribution) and in the asymptotic regime $\overline{f}$. Here we have used $T_{2y} = T_{1y} = 4keV$ for the perpendicular temperature of beams and $\beta_2 = -\beta_1 = 0.35$ for velocities. The results have been obtained with the 1D2V version of the semi-Lagrangian Vlem solver.

The self-organization here evidenced is driven by high wavenumber spatial fluctuations that are occurring both in the magnetic field and in the distribution function δf. They violate the constancy of the entropy S or of the L^2 norm because of the global coupling in wave vectors at separate spatial scales.

We finally note that in the numerical 1D2V Vlasov approach the exchange of momentum is related to the action of a differential operator $\partial/\partial p_y$, which, because of digitalization, must be approximated by some scheme on the discrete grid. The truncation errors induced by this approximation, and the subsequent numerical coarse graining process of the computed quantities, may affect the final result related to the process of phase-space filamentation (see Ref.[21] for a discussion) and finally results in growth of the Shannon's entropy. Another contribution may also come from the microscopic fluctuations of f. In order to separate the former "numerical artifact", which

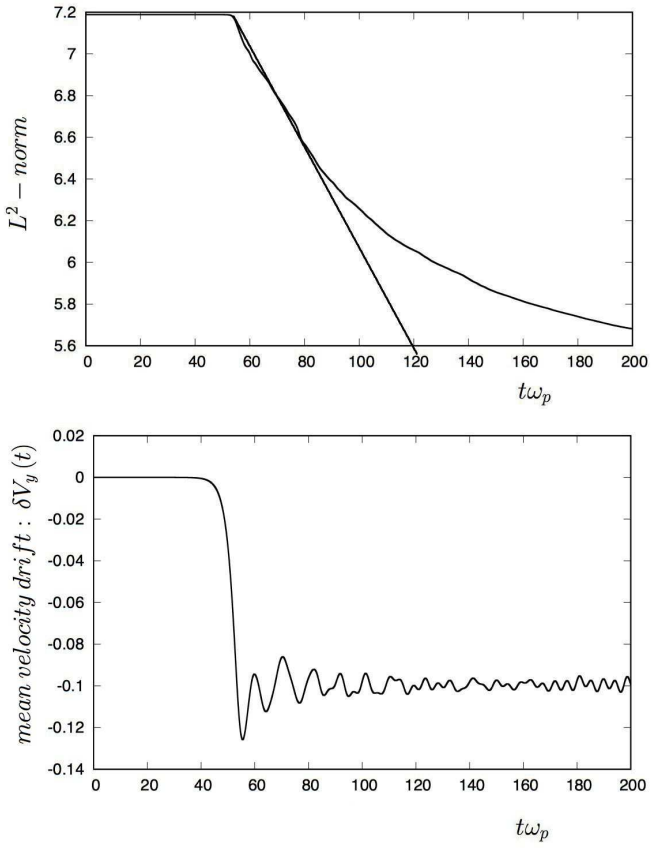

Figure 4. On top panel: the evolution of the L "entropy" (the L^2 norm) as a function of time. On bottom panel: the corresponding variation in mean velocity δV_y as a function of time. The simulation was carried out using the full kinetic 1D2V version (with two components in momenta). Here we have used $T_{2y} = T_{1y} = 4keV$ for the perpendicular temperature of beams and $\beta_2 = -\beta_1 = 0.35$ for velocities.

is due to coarse graining, from the analysis of momentum transfer due to microscopic fluctuations of f we can follow a more fundamental approach: we can use the multi-stream model, which is based on the exact invariance of the canonical momentum. In the MS model the description in p_y is based on an exact class of solutions, the perpendicular canonical momentum P_{cy}. This feature, on the one hand, gives rise to a new (macroscopic) topological constraint with respect to which we can interpret the momentum exchange process. On the other hand, this allows us to overcome the issues related to the numerical discretization of differential operators in the p_y coordinate, since bunches of "cold" particles (i.e., mathematically speaking, δ-of-Dirac particle distributions) are considered along this velocity direction.

4.1.2. CFI-WI coupling in the multi-stream approach The MS model allows a natural implementation of the "cold" CFI instability first considered by Fried [49]. As highlighted

by that author, this instability and the WI first devised in Ref.[50] are due to the same physical process and lead to an analogous amplification of the magnetic field. A formal equivalence between the cold CFI and warm WI can be indeed shown thanks to the multi-stream approach [18, 51, 52, 53]. When $kd_e \sim 1$, it is usually expected that the saturation of Weibel-type instability through magnetic trapping sets in, once the magnetic bounce frequency ω_B becomes comparable to the linear growth rate of the instabilities. The real situation can be however more complex than this, as it can be understood by noticing that a streaming plasma system, although warm, can be split into several particle "bunches" or "classes" (defined by the value of their local canonical invariant $\boldsymbol{P}_{c\perp}$) that experience different values of the bounce frequency ω_B, since the latter explicitly depends on $|\boldsymbol{P}_{c\perp}|$.

In the MS approach we can construct any equilibrium by selecting the appropriate value of the initial parameter $\boldsymbol{C}_j$ that identifies the stream, according to Eqs.(13-14). For this purpose, it is necessary to initialize the system in the form of a distribution function given by

$$f\left(x, p_x, p_y, t=0\right) = \sum_j \alpha_j f_j\left(x, p_x, t=0\right) \delta\left(p_y - C_j\right), \tag{27}$$

where α_j are normalization constants. For instance, we recover the cold CFI by selecting $N_s = 2$ streams located at $\boldsymbol{C}_j = \pm C_j \boldsymbol{e}_y$ where $C_{j=2,5} = \pm p_1$.

Concerning the WI, it is possible to take into account a perpendicular temperature for each beam considered in the cold CFI case. It is sufficient to attribute to each beam two "supplementary streams" located for example at $C_{j\neq 2,5} = \pm p_1 \mp \sqrt{3} m v_{Ty}$, where v_{Ty} is the thermal electron temperature along y.

In the numerical case we consider here, the two beams have velocities $v_{1,2} = \pm 0.35c$. The numerical integration of the MS model shows that only six streams are necessary to reproduce the beam-plasma system described in the previous subsection 4.1.1. Keeping the same densities and temperatures as before, that is, $n_1 = n_2 = n_0/2$ and $T_{1x} = T_{2x} = 2keV$, $T_{1xy} = T_{2y} = 4keV$, we obtain $\alpha_{j=2,5} = \frac{1}{3}$ for the "bulk plasma" and for the "beam" and $\alpha_{j\neq 2,5} = \frac{1}{12}$ for the auxiliary "streams" which allow us to take into account of temperature effects and so to describe the WI in the beam-plasma system. For the MS simulation we choose a time step of $\triangle t \omega_p = 0.005$ and a phase space sampling of $N_x N_{p_x} = 512^2$ grid points. The cut-off in the momentum space corresponds to $|p_x/mc| \leq 1.25$ and the box length is $L_x \omega_p / c = 2\pi$. The initial perturbation is given on the magnetic component B_z with a $\sin k_0 x$ perturbation with $k_0 c/\omega_p = 1$ and normalized amplitude $eB_0/m\omega_p = 10^{-5}$.

Numerical results are displayed in Figs. 5 and 6.

In Fig.5 we have shown the time evolution of some quantities. In the top panel, we have plotted the square root of the magnetic energy $\sqrt{\varepsilon_m}$. The essential features of the linear and nonlinear evolution of the magnetic energy obtained with full VM simulations in Sec. 4.1.1 are recovered by the reduced Hamiltonian code: the saturation level is identical to that displayed in Fig.1 and the magnetic bounce period T_B is found to be in good agreement with the expected value. In the middle panel in Fig. 5, we

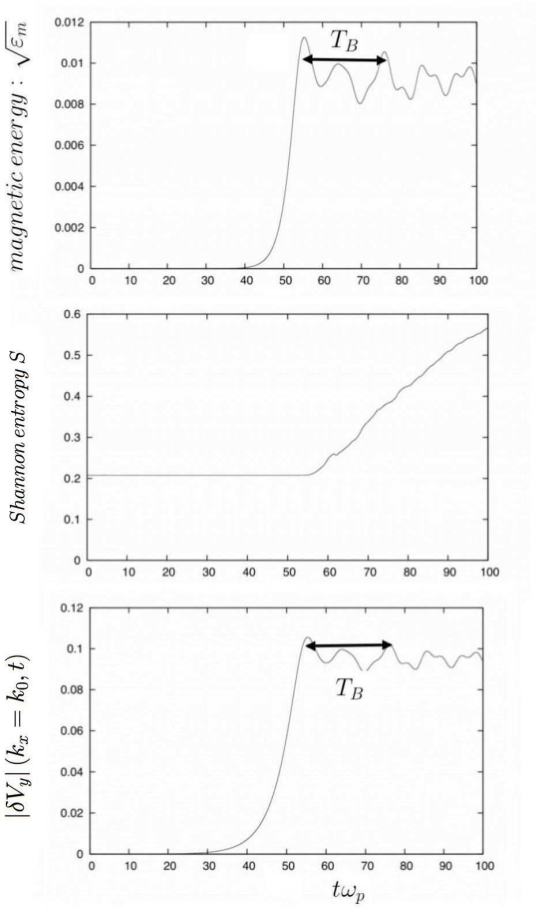

Figure 5. Top panel: plot of the square root of the magnetic energy $\sqrt{\varepsilon_m}$ versus time. The essential features of the linear and nonlinear evolution of the magnetic energy are recovered by the reduced Hamiltonian code (the multi-stream code) −cf. with Fig.1. Middle panel: entropy variation versus time. Bottom panel: momentum transfer involving the p_y component, triggered by the spontaneous microscopic fluctuations linked to the Shannon's entropy growth. The simulation has been carried out with the 1D1V multi-stream numerical model, and refers to the case discussed in Sec. 4.1.2. We have used $T_{2y} = T_{1y} = 4keV$ for the perpendicular temperature of beams and $\beta_2 = -\beta_1 = 0.35$ for velocities.

have plotted the Shannon's entropy S versus time: a linear growth of entropy takes place when the nonlinear regime of the saturation is reached.

The growth of δV_y results from a nonlinear breaking of the initial symmetry of the configuration and is allowed by the exact invariance of the canonical momentum P_{cy}, which imposes a topological constraint on the particle motion in phase space. Since $P_{cy} = p_y + eA_y\,(x,t) = const = C_j$, part of the momentum transfer is due to the pure electromagnetic component, the vector potential component A_y. For instance, from (19), we have $p_y \simeq C_{j=5} - eA_y = v_2 - eA_y$ and $\beta_y - \beta_2 \simeq -\frac{eA_y}{mc}$ and the total momentum

at time t is

$$\delta V_y = -\int eA_y \left[\overline{f}\left(\Gamma\right) + \left\langle \delta f\left(\Gamma/\Gamma_2\right)\right\rangle_{\Gamma_2}\right] d\Gamma$$
$$\simeq -\int eA_y\left(x,t\right)\sum_j \alpha_j n_j\left(x,t\right)\, dx, \tag{28}$$

where the summation $\sum_j$ is made over all "streams" j of density n_j.

In the bottom panel in Fig. 5 we have plotted the time evolution of the first Fourier mode $k = k_0$ of the variation of the mean "particle" velocity component $|\delta V_y\left(t\right)|$. We observe that the increase of δV_y is close to the numerical value obtained by the full-kinetic version of the code shown in Fig. 4 on bottom panel. This is in very good agreement with the analytical value given by Eq. (26).

The momentum transfer is caused by fluctuations that finally "violate" the global conservation of microscopic information given by the Shannon's entropy or by the L^2 -norm, while maintaining the invariance of other global quantities such as P_{cy}, the energy or the particle mass. The self-organization of the beam-plasma system occurs at saturation, in correspondence to the linear growth in time of the entropy (and the corresponding decrease of L not shown here).

The main process linked to the reorganization of the system begins with the emergence of a process of spatial filamentation involving the current densities, which is triggered by the CFI. We note that in the MS approach, each stream experiences its own bounce magnetic frequency and possesses its own topological constraint. Thus, the global interaction between streams may lead to some phase-mixing process. While in an ideal plasma the dynamics is constrained by an infinite number of topological constraints, the robustness of the solution obtained here in the way that the plasma self- organizes) is described by a small number of streams and their mutual interaction. Thus the MS model offers a conceptual framework for delineating and understanding the notion of self-organization which is simultaneous with entropy production. Although "numerical" dissipation is also present, a simple energy minimization variational principle is no longer appropriate, but it may still be possible to construct a variational relaxation model of plasma steady states by using the maximum entropy principle in strongly nonlinear systems. It should be noted that the MS numerical model is free from the computational burden, which in 1D2V VM simulations is due to the momentum resolution in p_y that is required to grant an accurate description of streams with low particle densities and large values of $|p_y|$. Populations of particles with large values of $|p_y|$ can be of course observed, although at a high computational cost, in full 1D2V VM simulations [53]. Despite they represent a small fraction of the particles involved in the CFI or WI, their importance is linked to the major role they can have in the saturation mechanism of these instabilities. An example of the efficiency of the MS model in following the nonlinear dynamics of these particle populations is shown in Fig. 6, where the evolution of a particle population which constitutes the stream with momentum $p_y = p_2 + \sqrt{3}mv_{Ty}$ is displayed: a detailed description of low density regions in phase space, especially of the tails of the distribution function where only a small number of

particles would be involved in particle-in-cell (PIC) or Vlasov simulation, is in this way made possible at a "fluid" computational cost, thanks to the constraint imposed by the conservation of the canonical momentum. This figure illustrates the formation of thin spatial filaments, triggered by the CFI, which are associated to large fluctuations of the distribution function. Such a phenomenon, initially generated in the coordinate space by the so-called filamentation instability, later involves also the velocity space and finally enters in competition with the well-known phase-space filamentation of the distribution function, an intrinsic feature of the Vlasov model.

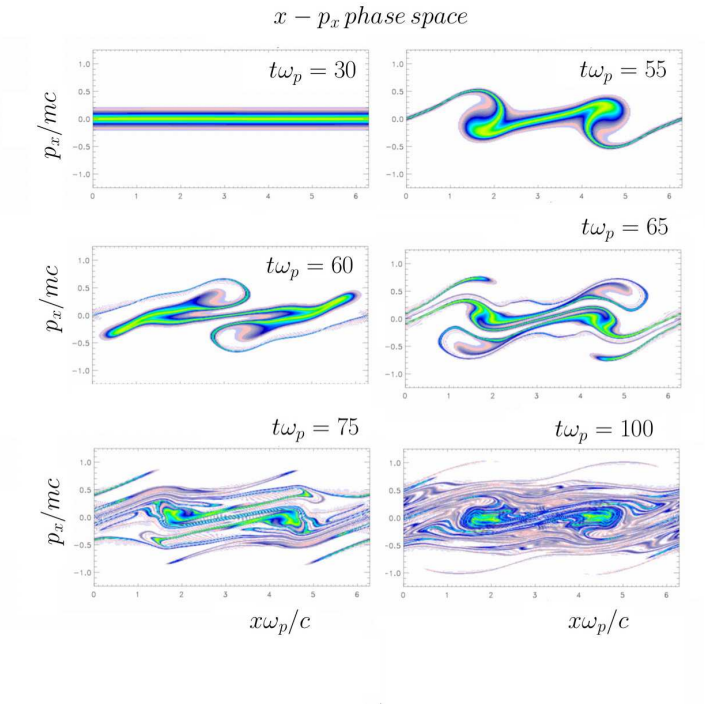

Figure 6. Contour-plot of f in the (x, p_x) space corresponding to the the "stream" with largest momentum and lowest particle density, considered in the MS case description discussed in Sec. 4.1.2. An average over the y and p_y coordinates has been performed. The physical parameters are the same of Fig. 5. The plot shows the formation of thinner and thinner filaments due to the CFI, which are associated to large amplitude fluctuations of the distribution function. The results have been obtained by integrating the MS model. We have used $T_{2y} = T_{1y} = 4keV$ for the perpendicular temperature of beams and $\beta_2 = -\beta_1 = 0.35$ for velocities (MS model).

While it is difficult in general to separate the different contributions that lead to the growth of the entropy (numerical coarse-graining effects induced by a numerical phase space grid of finite size from correlations driven by the statistical fluctuations) the situation is somewhat better when the multi-stream model is used, since this Hamiltonian reduction technique is based on the (mathematically) exact description of the transverse canonical momentum P_{cy} in the transverse direction and no sampling of the quantity p_y is used in this case.

Of course, even if the multi-stream model is built on a class of exact solutions

in the perpendicular direction (here denoted p_y), in the form of a superposition of Dirac distributions, and thus does not require any numerical approximation in this direction, the numerical inyegration in x and p_x also uses 2D spline interpolation for the determination of the feet of the characteristics. However, by reducing the dimensionality of the velocity space, the accuracy of the numerical semi-Lagrangian scheme is greatly increased, allowing a better estimation of the momentum transfer.

Unfortunately it is difficult to relate the observed growth of the Shannon's entropy to fluctuations of the distribution function from a analytical point of view. We will see that the L^2- norm is better suited for this calculation.

4.2. Momentum transfer in relativistic counter-streaming beams

It has been shown in Ref.[21], by studying the saturation of the OI, that a critical role in the saturation mechanism can be played by the contribution brought via the coupling with the TSI. The electrostatic field and the longitudinal spatial modulation of the plasma can therefore have great influence on the momentum transfer.

This time we consider a perturbation with oblique propagation with respect to the beam (i.e., $\boldsymbol{k} = k_x \boldsymbol{e}_x + k_y \boldsymbol{e}_y$), so to excite an OI, which has the contribution from both the CFI and TSI. From the numerical investigations that we are going to show it emerges that the self-organization of the beam-plasma system begins with the transfer of momentum, where kinetic effects induced by wave-particle resonances play a major role. Differently from the 1D2V CFI case studied in Sec. 4.1 and initialised with $\boldsymbol{k} = k_y \boldsymbol{e}_y$, the 2D2V case of the OI here considered is dominated by kinetic effects.

In order to deal with relativistic thermal spreads, each beam will be now represented by a drifting Maxwell -Juttner distribution function, whose general 3D expression is

$$f_{0j}\left(\boldsymbol{p}\right) = \frac{\mu_j}{4\pi\gamma_j^2 K_2\left(\frac{\mu_j}{\gamma_j}\right)} \exp -\mu_j \left(\gamma\left(\boldsymbol{p}\right) - \beta_j p_y\right), \tag{29}$$

where the index $j = \{1, 2\}$ labels the electron beam. Here β_j is the normalized drift velocity along y, γ_j is the corresponding Lorentz factor, $\mu_j = mc^2/(k_B T_j)$ is the normalized inverse temperature and K_2 is the modified Bessel function of the second kind. In the 2D momentum space considered here, the distribution function maintains a similar expression of type $f_{0j}\left(p_x, p_y\right) = A \exp -\mu_j \left(\gamma\left(p_x, p_y\right) - \beta_j p_y\right)$ where the modified normalized constant is computed assuming that, for each species j, $\iint f_{0j} dp_x dp_y = 1$.

We initialize the system with a plasma state dominated by the oblique filamentation instability for an initial wavenumber $kd_e \gtrsim 1$, for which a transition from the CFI to an OI with a large wavenumber component is expected. The linear analysis of the kinetic dispersion relation predicts the existence of a dominant oblique mode at $(k_x, k_y) = (0.4, 0.3)$ in ω_p/c units, for $n_1 = n_2 = n_0/2$, $\beta_1 = -0.745$ and $\beta_2 = +0.745$ (see for instance Ref. [9]). The initial distribution corresponds to two counter-propagating electron beams described by Eq. (29), for which we will consider different combinations of the beam temperatures. But for the results discussed in Sec. 4.2, the beam temperatures are in the range $T_1 = 10 - 20keV$ for one beam and are taken in the

range $T_2 = 1.5 - 2MeV$ for the second one. For all the runs shown in this subsection, a small perturbation in the magnetic field has been used so to assure a low initial level of magnetic-field fluctuations. Let us now discuss the results of the numerical experiments performed in the relativistic regime.

4.2.1. Study of the CFI-OI transition for low temperature beams Although we are ultimately interested in the transition to the OI for hot beam plasma configurations, we start the analysis by considering the counter-propagation of electron beams with moderate temperatures. For this first numerical simulation, we have chosen the temperatures $T_1 = 100keV$ and $T_2 = 500keV$. This choice has been done in order to reduce the linear growth-rate of the OI, so to allow a better description of the transition stage. It should be noted however that, even for the CFI instability alone, the asymmetry in the electron temperature induces a coupling of the CFI with electrostatic modes [54]. The size of the simulation box is given by $L_x \simeq 15.707c/\omega_p$ (which corresponds to a value of the fundamental wavenumber of $\Delta k_x = 2\pi/L_x = 0.40\omega_p/c$) and $L_y \simeq 20.943c/\omega_p$ (or equivalently to $\Delta k_y = 2\pi/L_y = 0.30\omega_p/c$ for the fundamental wavenumber in y).

In the first simulation case, the initial distribution function is perturbed by introducing magnetic fluctuations on the B_z component only, by exciting only the mode (n_x, n_y) equal to $(1, 1)$ in the Fourier space. In particular:

$$B_z = B_0 \sin\left(\Delta k_x x + \Delta k_y y + \varphi_{1,1}\right) \tag{30}$$

where the normalized value of the perturbation amplitude is $eB_0/m\omega_p = 0.0125$. The phase space sampling is given by $N_x N_y \times N_{p_x} \times N_{p_y} = 256^2 \times 128 \times 256$, for a total of 2.15×10^9 grid points, while the time step is $\Delta t\omega_p = 0.0075$. The intervals on the momentum components are defined by $|p_x/mc| \leq 20$ and $-20 \leq p_y/mc \leq 60$. Numerical results are plotted in Figs. 7 to 11.

In Fig. 7 we have shown, at two times, the $x - p_y$ phase space representation of the distribution function, averaged over the coordinate space y and the momentum component p_x. The top panel shows the initial f_0, while the bottom panel shows it just after the nonlinear saturation of the oblique instability, which takes place at a time close to $t\omega_p \simeq 50$ (see Fig. 8 for more details). Detailed analysis of fields dynamics in space reveals a kinetic coupling of the expected dominant mode (predicted by the linear kinetic dispersion relation to be $(k_x, k_y) = (0.4, 0.3)$ −see for instance Ref. [9])) with particles. This phase-space resonance occurs when $\omega \sim \boldsymbol{k}\cdot\boldsymbol{v}_j$. By contrast, filamentation modes with $\boldsymbol{k} \perp \boldsymbol{v}_j$ are purely growing, i.e., they have a real frequency $Re\,(\omega)$ close to zero.

Thanks to the Eulerian character of the code (which guarantees a very low level of numerical noise), it then becomes possible to accurately estimate the momentum transfer leading to a velocity variation due to the microscopic fluctuations of the "entropy" L, including in the case of relativistic temperatures. An approximation of the smoothed

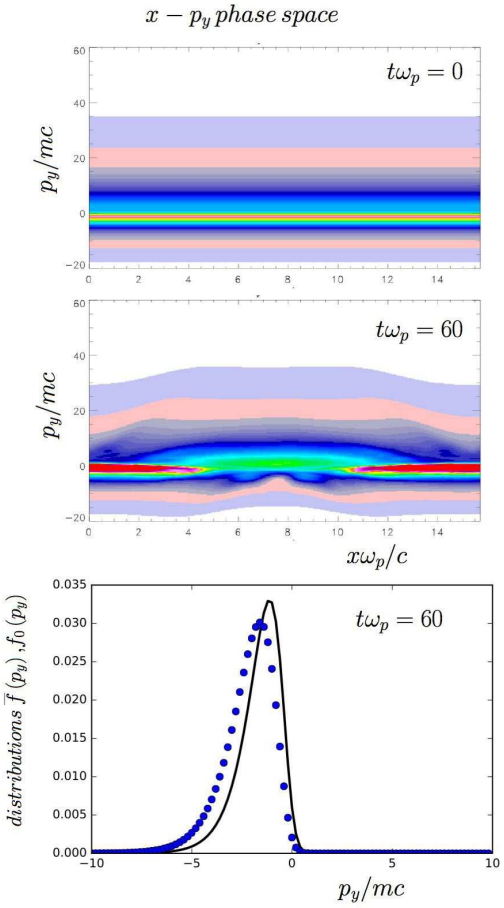

Figure 7. $x - p_y$ phase space representation of the distribution function at time $t\omega_p = 0$ (top panel) and just after the saturation at time $t\omega_p = 60$ (middle panel). An average over the y and p_x variables has been performed. On bottom panel, we have represented, from numerical data, the shape of the distribution of the cold beam by circles in comparison to the initial Maxwell-Jüttner distribution near $x\omega_p/c \sim 3$. The parameters are those of the case described in Sec. 4.2.1 corresponding to the perturbation (30) and the numerical results have been obtained with the 2D2V VLEM solver. We have used $T_1 = 100keV$ and $T_2 = 500keV$ for the relativistic beam temperatures and with $\beta_2 = -\beta_1 = 0.745$ for velocities.

distribution can be obtained by analyzing numerical data leading to:

$$\overline{f_1}(p_y) = \frac{\mu_1}{2}\left(\gamma(p_y) + \beta p_y\right) \times \frac{\mu_1}{4\pi\gamma_1^2 K_2\left(\frac{\mu_1}{\gamma_1}\right)} \exp -\mu_1\left(\gamma(p_y) - \beta_1 p_y\right), \quad (31)$$

or equivalently

$$\left.\frac{1}{f_0}\frac{\partial \overline{f}}{\partial \beta_y}\right|_{\beta_j} = \left.\frac{mc\overline{\gamma}^3}{f_0}\frac{\partial \overline{f}}{\partial p_y}\right|_{\beta_j} \sim \overline{\gamma}^3 \beta_j \mu_j, \quad (32)$$

and where $\overline{\gamma} = \int \gamma \overline{f}_j d^2p$ is a mean Lorentz factor (evaluated from the contribution of all particles of a given beam j).

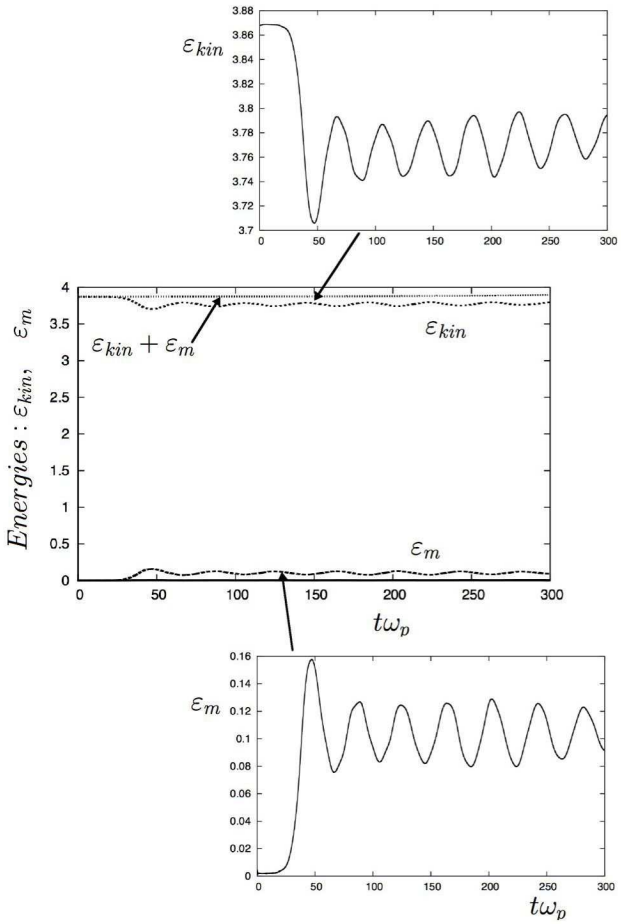

Figure 8. Time evolution of the kinetic energy ε_{kin}, of the magnetic energy ε_m and of their sum $\varepsilon_{kin} + \varepsilon_m$ represented together in the middle panel. The excellent conservation of $\varepsilon_{tot} = \varepsilon_{kin} + \varepsilon_m$, is allowed by negligibility of the electrostatic contribution $\varepsilon_e \ll 1$. Zooming onto the details of the kinetic and magnetic energies (top and bottom panels, respectively), we clearly observe an oscillatory energy transfer between these quantities. The parameters are the same of Fig.7, and the results have been obtained with the 2D2V VLEM solver. The simulation was performed with $T_1 = 100keV$ and $T_2 = 500keV$ for the relativistic beam temperature and with $\beta_2 = -\beta_1 = 0.745$ for velocities (normalized to the light velocity)

The time evolution of the kinetic energy $\varepsilon_{kin} = \int mc^2 (\gamma - 1) f(d^2x/V)d^2p$, of the magnetic energy $\varepsilon_m = \int (B_z^2/2\mu_0)(d^2x/V)$ (where $V = L_x L_y$ is the "volume" of the plasma box), and of their sum $\varepsilon_{kin} + \varepsilon_m$, are shown in the middle panel of Fig. 8. Zooms of the variation of the kinetic energy ε_{kin} and of the magnetic energy ε_m are shown in the upper and lower panel, respectively. The small amplitude initially chosen for the magnetic perturbation allows the growth of ε_m by several orders of magnitude before it reaches saturation. As it typically happens, the latter is characterized by an oscillatory exchange between the kinetic and magnetic energy components. When the unstable magnetic-field perturbation grows to a sufficiently large amplitude, we can

estimate the corresponding bounce frequency to be

$$\frac{\omega_B}{\omega_p} = \sqrt{\frac{|\boldsymbol{k}|\, c}{\omega_p}\, \frac{p_\perp}{mc\gamma^2}\, \frac{eB_{max}}{m\omega_p}} = \sqrt{3.02 \times 0.496 \times 0.7} \simeq 1.03 \tag{33}$$

In Eq.(33) the wavenumber and magnetic field amplitude have been evaluated from the numerical results, shown in Fig. 9. The frequency of the oscillation of the energy transfer displayed by the lower and upper panels of Fig. 8 is instead close to $\omega \simeq 0.16\omega_p$, a value smaller than the magnetic bounce frequency, and which can be related to the oscillating mechanism in the momentum transfer between the populations of particles of different temperatures. This result is quite general and has already been noted in a fluid context [55]. The oscillatory energy exchange between the source energy of an instability and the component to which it is converted, is indeed a typical feature of the instability saturation stage and, more generally, it is a general feature of the nonlinear dynamics of action-reaction system (e.g., of RC circuits). We recall in this regard that, in problems of merging of current patches [56] and of magnetic reconnection [57] in collisionless fluid plasmas, an energy exchange between the kinetic and the magnetic energy components, analogous to that observed in Fig. 8, here, has been related to the nonlinear oscillations of the perturbed magnetic structure (i.e., the current patch or the generated magnetic island). More specifically, by following Grasso et al. [58], in which a decomposition between coarse-grained and small scale fluctuations similar to that expressed by Eq.(A.4) has been performed for the fluid fields involved in the reconnection process, the period of energy fluctuations in the saturation stage of collisionless tearing modes has been discussed in Ref.[55] to correspond to spatial oscillations of the fluctuating fields. Such a result is analogous to the interpretation we have provided of the relation between the oscillation of the energy component (Fig. 8) and the fluctuations of the distribution function which are associated to the momentum transfer.

Notice also the excellent conservation of the total energy (within 0.5% of the initial value) displayed in Fig. 8. Moreover, in this regime of the interaction, the electric energy component $\varepsilon_e = \int 1/(2\varepsilon_0) E^2 (d^2x/V)$ remains negligible, which results in the familiar conservation relation of the total particle kinetic energy plus magnetic energy, already discussed in Ref.[23].

A second simulation has been run with identical parameters as before, but by exciting a superposition of several unstable modes, according to

$$B_z = \sum_{n_x, n_y = 1}^{10} B_0 \sin\left(n_x \Delta k_x x + n_y \Delta k_y y + \varphi_{n_x, n_y}\right). \tag{34}$$

The corresponding results are shown in Figs. 9-10. Fig. 9 displays the dynamics of the magnetic field component $eB_z/m\omega_p$ at three different times, while Fig. 10 illustrates the spatial modulation of the electric field components in space at the end of the simulation, $t\omega_p = 300$: the $eE_x/m\omega_p c$ component is shown on top panel, and the $eE_y/m\omega_p c$ component on bottom panel. It is clear from Fig. 9 that the system evolves towards a coupled oblique (OI) - filamentation (CFI) mode. In response to the unstable magnetic-field perturbation, here given on several modes, a $k_y \simeq 0$ mode emerges, attesting the

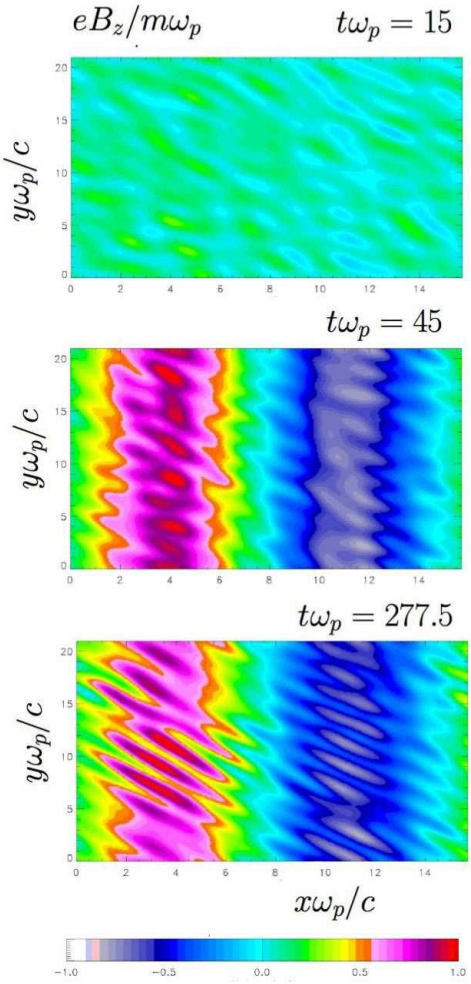

Figure 9. Contour-plot of the magnetic field $eB_z/m\omega_p$ at three times, showing the excitation and growth of a filamentation (CFI) instability. After a "linear" phase (in agreement with the linear dispersion relation) characterized by growth of fluctuations, the filamentation mode is observed on middle panel at time $t\omega_p = 45$, corresponding to saturation. An oblique mode also emerges, leading to strong fluctuations along y (visible in the bottom panel). The 2D2V simulation was performed with $T_1 = 100keV$ and $T_2 = 500keV$ for the relativistic beam temperature and with $\beta_2 = -\beta_1 = 0.745$ for velocities (normalized to the light velocity).

growth of CFI. As illustrated in Figs. 9 and 10, the CFI dominates the first stage of the instability. A close inspection of Fig. 9 (middle panel) shows the appearance of a dominant mode with $k_x = \Delta k_x$ (as expected) and $k_y \simeq 0$, together with the presence of fluctuations on k_y driven by the oblique mode.

The growth of such high wave-numbers fluctuations in the magnetic field is clearly observed at a later time, $t\omega_p \simeq 278$, on the bottom panel, in Fig. 9. A transition takes place later in time, as it is visible from Fig. 10, in the profile of the electric field

components. The system enters here into a new regime characterized by $kd_e \gg 1$ (small wavelengths). Also in this case the total energy (not shown) remains constant, within a 0.5% fraction of the initial value, throughout the duration of the simulation.

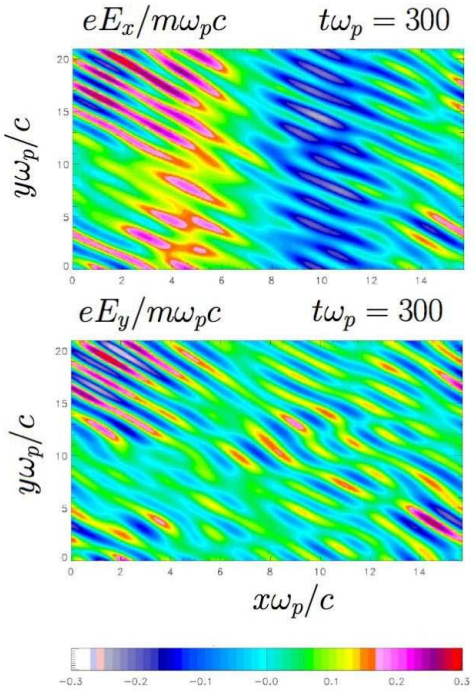

Figure 10. Contour-plots of the electric field components at the end of simulation: $eE_x/m\omega_p c$ is displayed on top panel and $eE_y/m\omega_p c$ on bottom panel. The transition from the filamentation mode to the oblique mode is observed. The parameters of this simulation are the same of Figs .8-9 and the 2D2V VLEM code has been used to obtain them. The simulation was performed with $T_1 = 100keV$ and $T_2 = 500keV$ for the relativistic beam temperature and with $\beta_2 = -\beta_1 = 0.745$ for velocities (normalized to the light velocity).

Changes in the features of the dominant OI mode, occurring when the transition takes place, can be seen in greater detail in Fig. 11. This figure shows the time evolution of the L^2-norm (i.e., of $\int d\Gamma \left(\overline{f}^2 + \langle \delta f \left(\Gamma/\Gamma_2\right)\rangle^2_{\Gamma_2}\right)$) together with some contour-plots of the distribution function in the (x, p_y) domain (f being averaged over the other coordinates, i.e. y and p_x). The amplitude of fluctuations with respect to the initial state can be quantified by $\delta L/L \sim 8\%$. After the saturation of the instability, a momentum transfer is observed in correspondence of the decrease of the L^2-norm. After an initial stage, where L is constant, L decreases in a linear way in time and $\delta L = \int d\Gamma \left\langle \delta f \right\rangle^2 \simeq \sigma t$. Using Eq. (21) we can estimate the resulting drift in mean velocity δV_y during the time

interval $\Delta_t = 160\omega_p^{-1}$:

$$\frac{\delta V_y}{c} = \frac{\sigma \Delta_t}{\frac{2}{f_0}\frac{\partial \overline{f}}{\partial \beta_y}\Big|_{\boldsymbol{\beta}=\beta_2}} \sim -\frac{0.0882 \times 160}{2 \times 88.2} = -0.08. \tag{35}$$

In Eq. (35) , we have estimated the parameter $\frac{1}{f_0}\frac{\partial \overline{f}}{\partial \beta_y}\Big|_{\boldsymbol{\beta}=\beta_2}$ by means of Eq. (32), using the velocity of the hot beam $\beta_2 = 0.745$, the hot beam temperature of $T_2 = 500keV$ and using the numerical estimate of the Lorentz factor $\overline{\gamma} \simeq 4.876$ (close to the relativistic energy $\epsilon_K + mc^2$ divided by mc^2). We have thus

$$\frac{1}{f_0}\frac{\partial \overline{f}}{\partial \beta_y}\Big|_{\boldsymbol{\beta}=\beta_2} \sim \frac{mc^2}{T_{y2}}\overline{\gamma}^3\beta_2 = \frac{511}{500} \times 4.876^3 \times 0.745 = 88.2,$$

which indeed corresponds to the value used in (35). In (35), $\overline{f}$ is normalized to $n_0\omega_p^2/m^2c^4$ while the "L^2-entropy" production rate can be estimated as $\sigma = \frac{L-L_0}{L_0} \simeq \frac{0.0124-0.0136}{0.0136} \simeq -8.82 \times 10^{-2}$ from the decrease of the L^2 norm observed in the top panel of Fig. 11. We also observe a local depletion of the distribution function located in the central region of the (x, p_y) domain, showing that the deformation of f takes place when L begins to decrease.

On bottom panel in Fig. 11, we have plotted the evolution of the mean velocity drift δV_y using the expression (25). In this Figure we have put the emphasis on the dynamics of the hot beam. After a transient phase, we observe that oscillations take place in the momentum transfer between the two populations of beam particles of different temperatures. The estimation of Eq.(35) is found to be in very good agreement with the mean value $\delta V_y \simeq 0.08c$ obtained from the data of the simulation.

4.2.2. Oblique instability in the relativistic temperature regime. Previous analytical works in the relativistic and ultra-relativistic regime [10, 20], based on the solution of the linear kinetic dispersion relation, have shown that a high enough beam temperature ($T_2 \gg 1keV$, for the case considered here) is a sufficient condition for the appearance of oblique modes: filamentation modes are seen to prevail up to temperatures $T_2 \sim 100keV$, whereas oblique modes clearly take over when $T_2 \sim 2MeV$.

In the simulation discussed in this Section we have thus increased the temperature of the "hot" beam (2) up to a relativistic temperature of T_2 and we have kept for the beam (1) (the "bulk, drifted plasma") a much lower value of T_1. The cases corresponding to two specific choices of temperatures are discussed in the following. The other physical parameters are unchanged in comparison to those used in Sec. 4.2.1, which are related to Figs. 7 to 11: $\beta_1 = -0.745$ and $\beta_2 = +0.745$ (the counter-propagating beams are symmetric in density and velocity); $L_x = 15.707c\omega_p^{-1}$ and $L_y = 20.943c\omega_p^{-1}$, which allow the excitation of an oblique mode with $k_x = \Delta k_x = 0.40\omega_p/c$ and $k_y = \Delta k_y = 0.30\omega_p/c$. The phase space sampling is given by $N_xN_y \times N_{p_x} \times N_{p_y} = 128^2 \times 128 \times 256$ points, the time step is $\Delta t\omega_p = 0.005$. The perturbation, in particular, has been given on a set of modes, namely $0 \leq k_xc/\omega_p \leq 4$ and $0 \leq k_yc/\omega_p \leq 3$, by using an equation like (34).

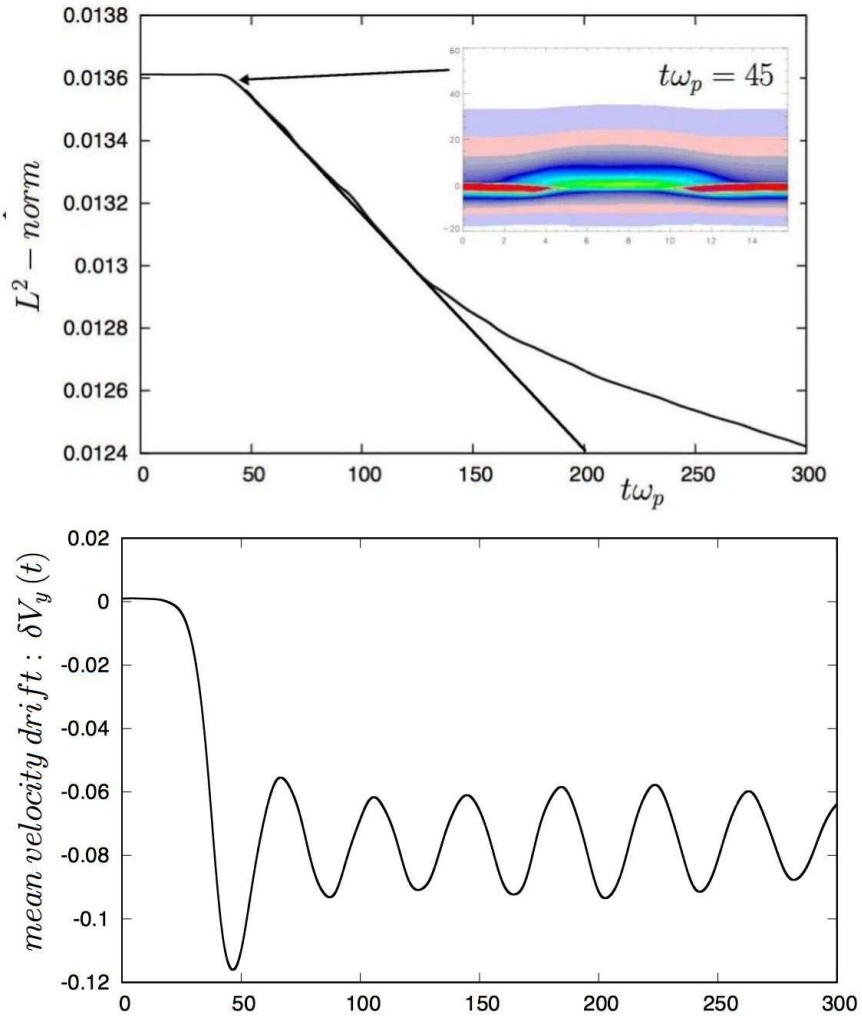

Figure 11. Illustration of the $x - p_y$ phase space of the distribution function together with the time evolution of the L^2 norm. "Hot" beam (mean) velocity variation, shown in bottom panel, is observed after saturation of CFI when the L^2 norm starts to decrease and when a higher wavenumber oblique mode is growing. Physical parameters used in the simulation are: $T_1 = 100keV$, $T_2 = 500keV$, $\beta_1 = -0.745$, $\beta_2 = +0.745$ for beams of equal densities $n_1 = n_2 = n_0/2$.

Let us discuss the dynamics of the oblique instability in the regime where $kd_e \gg 1$ by distinguishing two successive stages. In order to highlight some essential features in each of them, in the following we compare and complement the simulation results obtained for two different choices of the magnetic perturbation amplitude and of the beam temperatures. The latter are chosen to be $T_2 = 2MeV$ and $T_1 = 10keV$ in the first case and $T_2 = 1.5MeV$ and $T_1 = 20keV$ in the second one.

First stage: linear growth and saturation by magnetic trapping We first consider a run performed by setting $T_2 = 2MeV$, $T_1 = 10keV$ and $eB_0/m\omega_p = 10^{-3}$, and we focus on the initial stage dominated by the linear growth of the most unstable mode (as expected by the linear analysis to correspond to $(n_x, n_y) = (1, 1)$. This stage is followed by the nonlinear saturation which arises due to magnetic trapping.

In the middle panel of Fig. 12 it is shown, on logarithmic scale, the time evolution of the magnetic energy ε_m together with that of the x and y components of the electric energy ($\varepsilon_{e,x} = E_x^2/(2\varepsilon_0 m_e c^2)$ and $\varepsilon_{e,y} = E_y^2/(2\varepsilon_0 m_e c^2)$, in normalized units). Time oscillations at a frequency close to $\omega = kv_2 \simeq 0.375\omega_p$ are visible throughout the first stage of the instability. This corresponds indeed to a phase velocity of $v_\varphi \sim 0.695c$, close to v_2, which evidences the propagative character of the oblique mode.

The corresponding growth-rate is found to be $\eta/\omega_p \simeq 0.08$, a value close to the expected theoretical value of $\eta_{CFI-OI}/\omega_p = 0.07$. Significant changes in the topology of the generated magnetic field (shown on top panels of Fig. 12) is observed during the exponential growth of the modes. At saturation, the magnetic field exhibits a structure that is quasi-aligned along the y-direction, indicating a strong coupling between CFI and OI. Finally on bottom panel in Fig. 12 we have plotted the time evolution of the quantity L (the L^2- norm) which exhibits a strong decrease at saturation (of order of 1.5%).

Different phase-space projections of electron distribution function are shown in Fig. 13, at time $t\omega_p = 288$. We have displayed, respectively, the projection on the (p_x, p_y) plane (top panel), that on the (x, p_x) plane (middle panel) and that on the (x, p_y) plane (bottom panel). The top panel shows how the growth of the OI results in the di-symetrization of f in the momentum space because of the resonant character of the instability. As the amplitude of the self-generated magnetic field grows in time, the particle dynamics is strongly modified by the fields. As expected, the dominant mode is observed for (n_x, n_y) equal to $(1, 1)$ and $(1, 0)$, i.e. in the small wavenumber regime. Here the instability leads to the formation of a one-vortex structure both in the (x, p_x) and (x, p_y) phase space representation of the distribution function. The formation of this coherent structure clearly indicates that the saturation scenario is driven by magnetic trapping for this CFI-OI coupling. However, inside the vortex, the distribution function exhibits a strong filamentation which accompanies the momentum transfer. Magnetic trapping was early identified in Refs. [51, 52, 53], both theoretically and numerically, by using the invariance of the transverse canonical momentum, as the main mechanism responsible for quenching the progress of the phase-space filamentation.

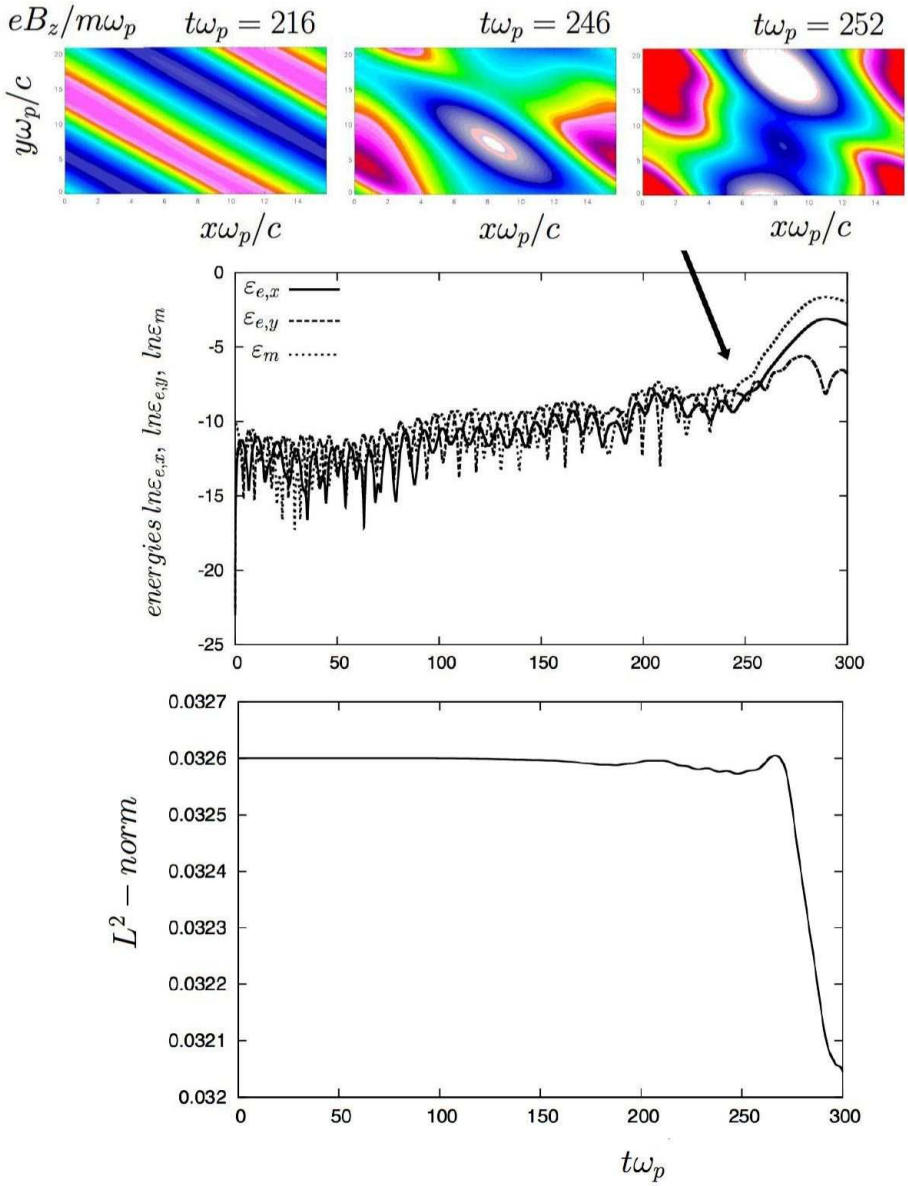

Figure 12. Illustration of OI in counter-propagating beam-plasma in the relativistic regime. The time evolution of magnetic energy ε_m, the component of the electric energy along x (ε_{ex}), the component of the electric energy along y (ε_{ey}) are shown in the bottom pattern, in logarithmic scale. The contour-plot of the generated magnetic field component, B_z, is shown on the top three panels at different times. The figure corresponding to $t\omega_p = 252$, in particular, evidences the CFI-OI coupling. On bottom panel, the corresponding time evolution of the $L-$"entropy". These results refer to the simulation case with $T_2 = 2MeV$, $T_1 = 10keV$ discussed in Sec. 4.2.2 and have been obtained with the 2D2V VLEM solver.

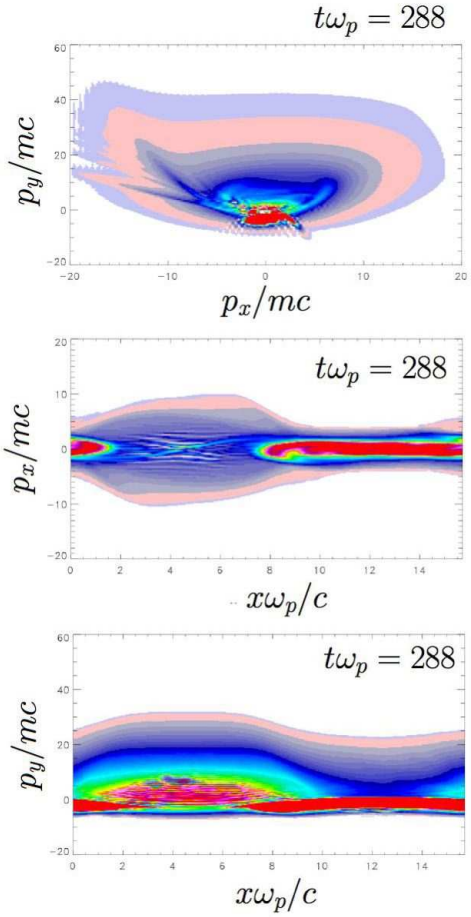

Figure 13. Representations of the electron distribution function at $t\omega_p = 288$ (that is, near saturation −cf. Fig. 11), in the (p_x, p_y) plane (top panel), in the (x, p_x) plane (middle panel) and in the (x, p_y) plane (bottom panel). In each case, an integration over the other variables has been performed. The di-symetrization of f induced by the resonant particle-wave interaction is visible in top panel, and a single vortex, corresponding to a magnetic trapping structure, is clearly observed in bottom panel. These results refer to the simulation case with $T_2 = 2MeV$, $T_1 = 10keV$ discussed in Sec. 4.2.2 and have been obtained with the 2D2V VLEM solver.

Second stage: momentum transfer at saturation We now focus on the momentum transfer which occurs at saturation in the relativistic regime of the instability. In order to highlight the momentum transfer mechanism, we consider here a second run performed for a longer time after the saturation arises. In order to maintain a satisfactory conservation of integral quantities over such a long time interval without changing the phase-space resolution, we have increased the perturbation amplitude to $eB_0/m\omega_p = 0.0125$ and we have slightly reduced the temperature difference between the two beams, by choosing their temperatures to be $T_2 = 1.5MeV$ and $T_1 = 20keV$. This represents a good compromise which allows us to maintain unchanged the essential features of the physical problem already discussed, with reference to Figs. 12 and 13.

In the middle panel of Fig. 14 is displayed the time evolution of the L^2-norm, which exhibits, after saturation, a decrease in time. The relative variation with respect to the initial value is about 2% at the end of the simulation. In the same figure, the contour-plots of the B_z magnetic field component are also represented on top panels. We see that an oblique mode is initially excited, but it is the filamentation mode (characterized by $k_y \simeq 0$) that becomes dominant at $t\omega_p = 240$. The trapping structures characterising the saturation of the OI (in correspondence to the decrease of the L^2-norm) in this regime are clearly observed at time $t\omega_p = 315$.

Despite the high temperature of one of the beams, the filamentation instability is strongly excited for such example of symmetric counter-propagating beams. We observe a re-organization of the magnetic field as the result of the growth of the dominant filamentation mode (i.e. with a wave vector component $k_y \simeq 0$) from the fluctuating magnetic noise introduced initially.

The projection of f on the plane (x, p_x) and on the plane (x, p_y) (after an average has been performed over over y and p_y, and over y and p_y) is represented at three different times in Fig.15. The emergence of a phase-space vortex, located at $x\omega_p/c \sim 10 - 14$ is visible in the (x, p_y) contour-plots (left panels of Fig.15). We see from this figure that the further decrease of the norm L^2 is also linked to the generation of thin filaments inside of the phase-space vortex, both in the (x, p_x) and (x, p_y) phase-space representations.

The natural coupling between CFI and high-frequency OI modes leads to a filamentation that induces a kinetic heating: we see from Fig.15 that the high-wavenumber OI modes give rise to thin filaments in the coordinate space, in the region of the first beam (the beam (1), or the "bulk drifted plasma") of velocity $v_1 \leq 0$ and contribute to the "heating" of the hot beam by momentum transfer in an asymmetric way (no momentum is deposed in regions of negative momentum, in Fig. 15). When the perturbed magnetic field reaches a sufficiently large amplitude, close to $eB_{max}/m\omega_p \sim 0.45$, the system enters a regime where magnetic trapping dominates, with a frequency close to

$$\frac{\omega_B}{\omega_p} = \sqrt{\frac{|\boldsymbol{k}|\, c}{\omega_p}\, \frac{p_\perp}{mc\gamma^2}\, \frac{eB_{max}}{m\omega_p}} = \sqrt{0.5 \times \frac{1}{5^2} \times 0.45} \simeq 0.095. \tag{36}$$

This value is comparable to the linear growth-rate, here measured to be $\eta \simeq 0.07\omega_p$. Once the system enters this regime (where $kd_e \sim 1$), magnetic trapping becomes the dominant saturation mechanism. It is then reasonable to expect that the magnetic-field will e-fold once or twice before saturating in a time that a particle takes to execute one bounce in the magnetic field trapping structure. As evidenced by Fig. 14, this process is associated to a momentum transfer. However, due to the importance of trapping effects, a quasilinear model can not be used to describe the momentum transfer. From the bottom panel in Fig. 14, an estimate of δV_y during the time interval $\Delta_t = 200\omega_p^{-1}$ leads to

$$\frac{\delta V_y}{c} = \frac{\sigma \triangle_t}{\frac{2}{f_0}\frac{\partial \overline{f}}{\partial \beta_y}\Big|_{\boldsymbol{\beta}=\beta_2}} \sim \frac{-0.272 \times 200}{2 \times 254} \simeq -0.10 \tag{37}$$

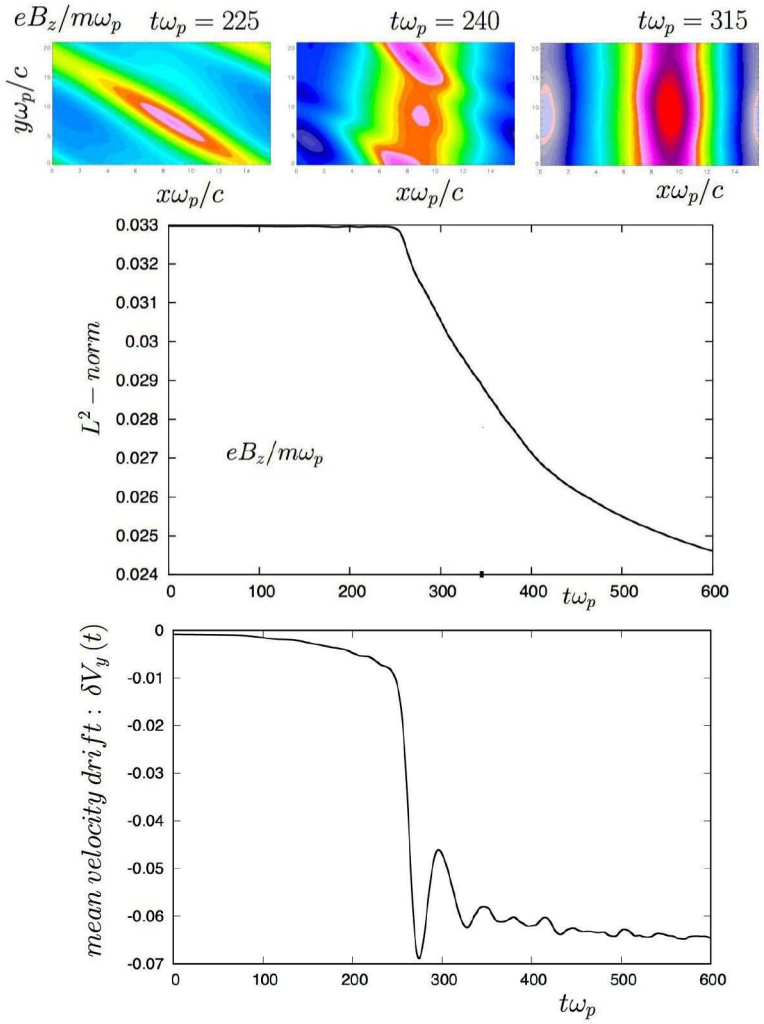

Figure 14. In the middle panel: time evolution of the L^2-norm. Its total relative variation is 2%. Contour-plots of the magnetic field are shown in lower and upper panels, at different times. On top panels, the re-organization evidences the coupling between an initially dominating an oblique mode and a filamentation mode (characterized by $k_y \simeq 0$) that becomes dominant at $t\omega_p = 240$. On middle panel, the asymptotic behavior shows the emergence of a magnetic trapping structure. On bottom panel we have plotted the variation δV_y in the mean velocity for the hot beam as a function of time. These results refer to the 2D2V Vlasov simulation with $T_1 = 20keV$ and $T_2 = 1.5MeV$. The corresponding beam velocities are $\beta_2 = -\beta_1 = 0.745$.

Here we have $\frac{1}{f_0}\frac{\partial \overline{f}}{\partial \beta_y} \simeq \overline{\gamma}^3 \mu_2 \beta_2 \sim 10^3 \times \frac{511}{1500} \times 0.745 \simeq 254$ while the "entropy" (L) production rate can be estimated as $\sigma = \frac{L-L_0}{L_0} \simeq \frac{0.024-0.033}{0.033} \simeq -0.272$ for a plasma temperature of $T_2 = 1500keV$.

Finally we present in Fig. 16 the corresponding time evolutions of the total energy on top panel and of the Shannon's entropy S on bottom panel, respectively. The result in (37) is somewhat larger when compared with the numerical value (here, again, estimated to be close to $\delta V_y \sim -0.06c$ as shown in the bottom panel in Fig. 14). This

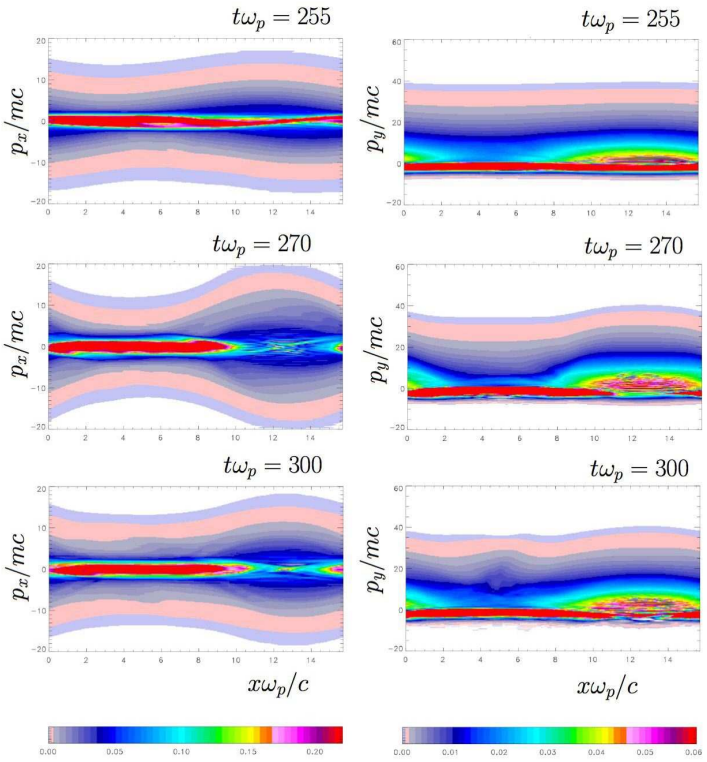

Figure 15. Contour-plots of $f(x, p_x)$ (left panels), and of $f(x, p_y)$ (right panels). An average over the other variables has been performed. Note that the decrease of the norm L^2 is linked to the generation of thin filaments inside of the phase-space vortex, both in the (x, p_x) and (x, p_y) planes. These results refer to the 2D2V Vlasov simulation with $T_1 = 20keV$ and $T_2 = 1.5MeV$. The corresponding beam velocities are $\beta_2 = -\beta_1 = 0.745$.

discrepancy is due to the finite size of the interval in the momentum coordinates and to its sampling. This discrepancy must be compared with the 17% total relative variation of the entropy S, which occurs while the total energy is very well conserved (0.85% in relative variation). As previously mentioned in Ref. [21], the Shannon's entropy exhibits four different steps during its evolution: after a constant phase, the entropy increases and reaches its saturation level, here at time $t\omega_p \sim 300$. Finally the entropy decreases as a result of the effects related to the second order fluctuations of f. This process, observed in the temporal dynamics of the Shannon's entropy, suggests that the first entropy increase, observed at the beginning of the instability has also occurred in an almost reversible way, again due to large amplitude fluctuations of f related to the OI. Thus we may expect that a little amount of microscopic information is irreversibly lost due to the combined effects of filamentation and numerical coarse-graining during the growth of the unstable oblique modes, while macroscopic information can be finally recovered later in time, in a similar way to what happens for plasma echoes.

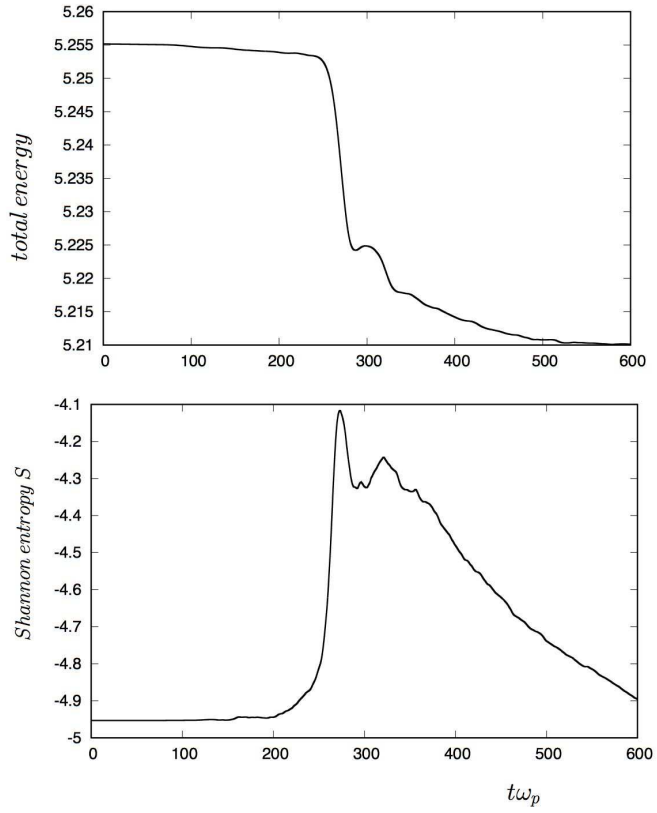

Figure 16. On top panel the time evolution of the total energy which remains constant within 0.8%. On bottom panel the corresponding time evolution of the Shannon's entropy S. These results refer to the 2D2V Vlasov simulation with $T_1 = 20keV$ and $T_2 = 1.5MeV$. The corresponding beam velocities are $\beta_2 = -\beta_1 = 0.745$.

5. Conclusion

In this article we have presented an analytical modelling and interpreted numerical experiments, performed with a Vlasov Maxwell solver in one and two spatial dimensions, aimed to study the momentum transfer associated to fluctuations of the distribution function in Weibel-type filamentation instabilities, both in classical and relativistic temperature regimes. In the different simulation runs here discussed, the energy exchange between the magnetic part and the plasma (kinetic energy) displays an oscillatory behavior that can be related to the dynamics of fluctuations at microscopic scales. An excellent energy conservation is verified throughout each simulation experiment, even in the large kd_e regime where fluctuations of the distribution function in the phase-space and fluctuations of the magnetic (or electric) field in the coordinate space are important.

Moreover, it is found that a net momentum transfer between the beams takes place, which in the problems addressed here can be "measured" to be related to an "entropy" production rate (corresponding, e.g., to a decrease of the L^2 norm). Although

a numerical, dissipative coarse graining can take part in this process by providing an irreversible entropy increase, we have shown the latter to be small with respect to the entropy increase which appears to be of *reversible* nature. We have then analytically shown this be compatible with the occurrence of the microscopic fluctuations of the distribution function, which are related to the momentum exchange between the beams. This result is significant since it demonstrates that the saturation level of the magnetic field generated by the instability of two counter-propagating electron beams is not only due to magnetic trapping but also depends on the conservation of the so-called Casimir's invariants, as for instance the L^2 norm, $L = \int d^2x d^2p f^2$, or on Shannon's entropy. This occurs when the re-organization of the system takes place. In particular, the energy transfer between the magnetic field and the particles, through the kinetic part of the energy, may oscillate in an adiabatic way, and a conversion between Casimirs like the "entropy" of the two beams and between their mean momenta is made possible. This conversion can take place when the oblique instability leads to the excitation of high wavenumber modes, which amplify, via filamentation in the coordinate space, the phase-space filamentation which is induced by the free streaming term in Vlasov equation. This process modifies the mathematical properties of f in term of regularity and weak convergence and therefore affects the saturation of the instability in the limit of small wavelengths.

Acknowledgment

The authors are grateful to the IDRIS computational center, Orsay, France, for computer time allocation on their computers. This work was granted across to the HPC resources (Grant 2019- 2020- 057290) made by GENCI (Grand Equipement National de Calcul Intensif)

Appendix A: Fluctuations of the single particle distribution, binary correlations and entropy fluctuations

In the Vlasov model, we write the two-particle distribution function as $f_2(\Gamma_1, \Gamma_2, t) \simeq f_1(\Gamma_1, t) f_1(\Gamma_2, t)$, where $\Gamma_1 = (\boldsymbol{x}_1, \boldsymbol{p}_1)$ and $\Gamma_2 = (\boldsymbol{x}_2, \boldsymbol{p}_2)$ denote the location and momentum of two particles (1) and (2) at a time t. Here f_1 is the usual one-particle distribution function usually met in the Vlasov equation in (3). Since the product $f_2(\Gamma_1, \Gamma_2, t)\, d\Gamma_1 d\Gamma_2$ represents the probability that the particle "one" be in the domain volume $d\Gamma_1$ around the point Γ_1, granted that the particle "two" be in the volume $d\Gamma_2$ around the point Γ_2, the mean field assumption is equivalent to say that the particles are statistically independent.

It must be noted in this regard that the lack of binary correlations in a Vlasov model coincides with the negligibility of binary collisions and is unrelated to the notion of thermodynamical equilibrium: setting to zero the collision operator in Vlasov equation follows from the mean field theory once it is a posteriori proven that $f_2(\Gamma_1, \Gamma_2, t) - f(\Gamma_1, t) f(\Gamma_2, t) \simeq O(g)$, where $g = (n_e \lambda_D^3) \to 0$ is the number of electrons with volume density n_e that are contained inside a microscopic sphere with a radius of

the order of the Debye length λ_D (see, e.g., [34], Ch. 7). In Boltzmann's theory of a perfect gas, instead, the same writing $f_2(\Gamma_1, \Gamma_2, t) = f_1(\Gamma_1, t) f_1(\Gamma_2, t)$ expressing the lack of binary correlations is valid when the number of collisions in a mesoscopic volume is sufficiently large (molecular chaos hypothesis) and, because of this, it is directly related to the closeness of the system to thermodynamical equilibrium conditions.

The presence of fluctuations of the particle distribution at microscopic scales gives rise to binary correlations among particles, which can be quantified by writing

$$f_2(\Gamma_1, \Gamma_2, t) = \overline{f_1}(\Gamma_1, t)\, \overline{f_1}(\Gamma_2, t) + \delta f_1(\Gamma_1/\Gamma_2, t)\, \overline{f_1}(\Gamma_2, t), \tag{A.1}$$

where:

- the symbol $\overline{f}$ indicates the part of the single particle distribution that possesses the regularity property discussed in Sec. 2 at point (iii); that is, $\overline{f}$, is the "smoothed" part of f.
- $\delta f_1(\Gamma_1/\Gamma_2, t)\, d\Gamma_1$ is the conditional probability that a fluctuations of f_1 with respect to its "regular" value $\overline{f}_1$ occurs for a particle (1) located at Γ_1 because of the presence of a particle (2) located at Γ_2. This correlation is triggered by the global character of the inter-particle interactions which is induced, for example, by turbulence. The mean field assumption is then equivalent to say that the two particles are statistically independent, which translates into $\delta f_1(\Gamma_1/\Gamma_2, t) = \delta f_1(\Gamma_1, t) \to 0$.

Averaging the distribution f_2 over Γ_2 then leads to

$$\langle f_2 \rangle_{\Gamma_2} \equiv \int d\Gamma_2 f_2(\Gamma_1, \Gamma_2, t) = \overline{f_1}(\Gamma_1 t) + \langle \delta f_1(\Gamma_1/\Gamma_2, t) \rangle_{\Gamma_2} \tag{A.2}$$

In Eq. (A.2) we have used the normalization condition $\int d\Gamma_2 \overline{f_1}(\Gamma_2, t) = 1$ and the definition

$$\langle \delta f_1(\Gamma_1/\Gamma_2, t) \rangle_{\Gamma_2} \equiv \int d\Gamma_2 \delta f_1(\Gamma_1/\Gamma_2, t)\, \overline{f_1}(\Gamma_2, t) \tag{A.3}$$

We so assume that the solution of the Vlasov equation can be written in the form

$$f(\Gamma_1) = \overline{f}_1(\Gamma_1) + \langle \delta f_1 \rangle_{\Gamma_2}. \tag{A.4}$$

We can now define an "entropy-like" function L_2 related to the two-particle distribution f_2 as

$$L_2 \equiv \int d\Gamma_1 \langle f_2 \rangle_{\Gamma_2}^2, \tag{A.5}$$

where

$$\langle f_2 \rangle_{\Gamma_2}^2 = \overline{f_1}^2(\Gamma_1, t) + \langle \delta f \rangle_{\Gamma_2}^2 + 2\overline{f_1}(\Gamma_1, t) \langle \delta f_1(\Gamma_1/\Gamma_2, t) \rangle_{\Gamma_2}. \tag{A.6}$$

Assuming that the L^2-norm of the two-particle distribution function is conserved, we obtain

$$\frac{\partial L_2}{\partial t} = -2 \frac{\partial}{\partial t} \int d\Gamma_1 \overline{f_1}(\Gamma_1, t)\ \langle \delta f_1(\Gamma_1/\Gamma_2, t) \rangle_{\Gamma_2}. \tag{A.7}$$

The expression of the total L^2 norm of Eq.(A.7) can be split as

$$L_2 = L(\overline{f_1}) + \delta L, \tag{A.8}$$

where

$$L\left(\overline{f_1}\right) \equiv \int d\Gamma_1 \overline{f_1}^2 \left(\Gamma_1, t\right) \ , \qquad \delta L \equiv \int d\Gamma_1 \left\langle \delta f_1 \left(\Gamma_1/\Gamma_2, t\right)\right\rangle_{\Gamma_2}^2 \tag{A.9}$$

An analogous result to Eq.(A.7) holds for the Shannon entropy and for any other convex entropy-like functional of f. In Ref. [21] it has been shown how such a mechanism of entropy production (and reduction) can occur reversibly and can dominate the well known irreversible entropy increase that in a numerical Vlasov model is encountered due to coarse-graining, when a phase-space filament reaches the size of the elementary cell of the numerical phase space grid.

It must be pointed out that such violation of the entropy was already evidenced to occur in Hamiltonian system with a small number of degrees of freedom and has been formalized in terms of the "*entropy production and fluctuation theorem*" in nanotechnologies [26, 27]. The L^2-norm, here denoted by the symbol L provides also a measure of the momentum transfer triggered by the fluctuation level.

More in general, Casimir invariants, of which entropy-like functionals are an example, can be interpreted as the statement of some topological constraint on the particle dynamics, that is, as the expression of the constancy in time of some microscopic quantity. The link between topological constraints related to Casimirs and microscopic conservations having a "collective", fluid counterpart is well known for example in the Hamiltonian fluid description of plasmas − see, e.g. Ref.[28] and, more specifically, Refs.[29, 30] for applications to magnetic reconnection. These microscopically conserved quantities can be affected by the emergence of strong fluctuations of the distribution function, a process that can be observed in turbulence. It should be noted that an analogous scenario is well known also in gyrokinetic modelling, when one separates the different spatial and time scales in the $\boldsymbol{J} - \boldsymbol{\alpha}$ action-angle variables description, while assuming the adiabatic invariance of the $\boldsymbol{J}$ action. The unfreezing of a given adiabatic invariant occurs when a sufficient level of small-scale perturbations violates the adiabatic condition (see Refs. [31, 32]). Similarly, small scale spatial fluctuations of a fluid, turbulent magnetized plasma can break the conservation of the magnetic moment and thus invalidate the double-adiabatic closure assumption in extended fluid models [33].

[1] Liu W, Li H, Yin L, Albright B J, Bowers K J, Liang E P 2011 *Phys. Plasmas* **18**, 052105.
[2] Schoeffler K M, Loureiro N F, Fonseca R A, Silva L O 2016 *Phys. Plasmas* **23**, 056304.
[3] Norreys P A, Beg F N, Sentoku Y, Silva L O, Smith R A, Trines R M G M 2009 *Phys. Plasmas* **16**, 041002.
[4] Bret A, Stockem A, Fiuza F, Ruyer C, Gremillet L, Narayan R, Silva L O 2013 *Phys. Plasmas* **20**, 042102.
[5] Cerutti B, Werner G R, Uzdensky D A, Begelman M C 2014 *Phys. Plasmas* **21**, 056501.
[6] Tamburini M, Pegoraro F, DePiazza A, Keitel C H , Macchi A 2010 *New J. Phys.* **12**, 123005.
[7] Lehmann G, Spatschek K H 2012 *Phys. Rev. E* **85**, 056412.
[8] Califano F, Pegoraro F, Bulanov S V, 1997 *Phys. Rev. E* **56**, 963.

[9] Bret A, Gremillet L, Bénisti D 2010 *Phys. Rev. E* **81**, 036402.
[10] Bret A, Gremillet L, Bénisti D, Lefebvre E 2008 *Phys. Rev. Lett.* **100**, 205008.
[11] Bret A, Gremillet L, Dieckmann M E 2010 *Phys. Plasmas* **17**, 120501.
[12] Diperna R J and Lions P L 1989 *Comm. Pure and Appl. Math.* **42**, 729.
[13] Villani C 2014 *Phys. Plasmas* **21**, 030901.
[14] Rein G 2004 *Comm. Math. Sci.* **2**, 145.
[15] Ghizzo A, Sarrat M, Del Sarto D 2017, *J. Plasma Phys.* **83**, 705830101.
[16] Huang K 1987 *"Statistical Mechanics"*, Wiley & Sons Ed., New York (NY).
[17] Inglebert A. , Ghizzo A., Reveille T., Del Sarto D., Bertrand P., Califano F. 2011 *Euro. Phys. Letters* ***95***, 45002.
[18] Inglebert A., Ghizzo A., Reveille T., Bertrand P., Califano F. 2012 *Plasma Phys. Control. Fusion* **54**, 085004.
[19] Pegoraro F, Bulanov S V, Califano F, Lontano M 1996 *Phys. Scr.* **T63**, 262.
[20] Ghizzo A, Del Sarto D, Sarrat M 2020, *Phys. Plasmas* **27**, 072103.
[21] Ghizzo A, Del Sarto D 2020 *Phys. Plasmas* **27**, 072104.
[22] Alfven H 1939 *Phys. Rev.* **55**, 425.
[23] Davidson R C, Hammer D A, Haber I, Wagner C E 1972 *Phys. Fluids* **15**, 317.
[24] Grassi A, Grech M, Amiranoff F, Pegoraro F, Macchi A, Riconda C 2017 *Phys. Rev. E* **95**, 023203.
[25] Medvedev M V, Loeb A 1999 1999 *The Astro. Journal* **526**, 697.
[26] Jarzynski C 1997 *Phys. Rev. E* **56**, 5018.
[27] Crooks G E 1999 *Phys. Rev. E* **60**, 2721.
[28] Morrison P J 1998 *Rev. Mod. Phys.* **70**, 467.
[29] Schep T J, Pegoraro F, Kuvshinov B N 1994 *Phys. Plasmas* **1**, 2843.
[30] Pegoraro F, Kuvshinov B N, Rem J, Schep T J 1997 *Adv. Space Rev.* **19**, 1823.
[31] Yoshida Z. 2016 *Advances in Physics* **1**, 2.
[32] Yoshida Z. and Mahajan S.M. 2014 *Prog. Theor. Exp. Phys.* 073J01.
[33] Del Sarto D, Pegoraro F 2016 *Comptes-rendus de la* 21^e *Rencontre du Non Linéaire*, Vol. 21, Ed. Falcon E, Lefranc M, Pétrélis and Pham C T (Paris), p.7
[34] Krall N A and Trivelpiece A W, 1973, *"Principles of Plasma Physics"*, McGraw-Hill Ed., New York (NY).
[35] Diamond P H, Itoh S I and Itoh K 2010 *Modern Plasma Physics, Vol. 1 Physical kinetics of turbulent plasmas* (Cambridge Uni. Press).
[36] Connaughton C, Nazarenko S, Quinn B 2011 *Eur. Phys. Lett.* **96**, 25001.
[37] Del Sarto D, Pegoraro F, Califano C 2016 *Phys. Rev. E* **93**, 053203.
[38] Del Sarto D, Pegoraro F 2018 *MNRAS* **475**, 181.
[39] Malkov M A, Diamond P H Rosenbluth M N 2001 *Phys. Plasmas* **8**, 5073.
[40] Ghizzo A, Del Sarto D, Palermo F, Biancalani A 2017 *Eur. Phys. Lett.* **119**, 15003.
[41] Kosuga Y and Diamond P H 2011 *Phys. Plasmas* **18**, 122305.
[42] M. Sarrat, A. Ghizzo, D. Del Sarto, L. Serrat 2017 *Eur. Phys. J. D* **71**, 271.
[43] Lazar M., Schlickeiser R., Shukla P.K. 2006 *Phys. Plasmas* **13**, 102107.
[44] Yoon P.H. 2007 *Phys. Plasmas* **14**, 064504.
[45] Tautz R.C. and Shalchi A. 2008 *Phys. Plasmas* **15**, 052304.
[46] Tautz R.C. and Schlickeiser R. 2007 *Phys. Plasmas* **14**, 102102.
[47] Bret A, Firpo M C, Deutsch C 2005 *Phys. Rev. Lett.* **94**, 115002.
[48] Gremillet L, Bénisti D, Lefebvre E, Bret A 2007 *Phys. Plasmas* **14**, 040704.
[49] Fried B D 1959 *Phys. Fluids* **2**, 337.
[50] Weibel E W 1959 *Phys. Rev. Lett.* **2**, 83.
[51] Ghizzo A, Bertrand P 2013 *Phys. Plasmas* **20**, 082109.
[52] Ghizzo A 2013 *Phys. Plasmas* **20**, 082110.
[53] Ghizzo A 2013 *Phys. Plasmas* **20**, 082111.
[54] Sarrat M, Del Sarto D, Ghizzo A 2016 *EuroPhys. Lett.* **115**, 45001.

[55] Del Sarto D, Califano F, Pegoraro F 2006 *Mod. Phys. Lett. B* **20**, 931.
[56] Bergmans J, Schep T J 2001 *Phys. Rev. Lett.* **87**, 19.
[57] Del Sarto D, Califano F, Pegoraro F 2005 *Phys. Plasmas* **12**, 012317.
[58] Grasso D, Califano F, Pegoraro F, Porcelli F 2001 *Phys. Rev. Lett.* **86**, 5051.